Multifunctional Energy Storage Composite Structures with Embedded Lithium-ion Batteries

Purim Ladpli[a†], Raphael Nardari[a], Fotis Kopsaftopoulos[b], Fu-Kuo Chang[a]

[a] Department of Aeronautics and Astronautics, Stanford University, Stanford, CA 94305, USA

[b] Department of Mechanical, Aerospace and Nuclear Engineering, Rensselaer Polytechnic Institute, Troy, NY 12180, USA

Abstract

This work proposes and analyzes a structurally-integrated lithium-ion battery concept. The multifunctional energy storage composite (MESC) structures developed here encapsulate lithium-ion battery materials inside high-strength carbon-fiber composites and use interlocking polymer rivets to stabilize the electrode layer stack mechanically. These rivets enable load transfer between battery layers, allowing them to store electrical energy while also contributing to the structural load carrying performance, without any modifications to the battery chemistry. The design rationale, fabrication processes, and experimental mechano-electrical characterization of first-generation MESCs are discussed. Experimental results indicate that the MESCs offer electrochemical performance comparable to standard lithium-ion cells, despite the disruptive design change. The mechanical performance of MESCs is assessed via quasi-static three-point bending tests, with results showing significantly improved mechanical stiffness and strength over traditional pouch cells. The rivets minimize interlayer shear movement of the electrode

† Corresponding author. Email: pladpli@stanford.edu; Address: Durand Building, Room 054, 496 Lomita Mall, Stanford University, Stanford, CA 94305, USA; Tel.: +1 (650) 723-3524.

stack, thus allowing it to maintain electrochemical functionalities while carrying mechanical bending. While minimal load application can cause permanent deformation of pouch cells, MESCs maintain their structural integrity and energy-storage capabilities under realistic repeated loading. The results obtained demonstrate the mechanical robustness of MESCs, which allow them to be fabricated as energy-storing structures for electric vehicles and other applications.

Keywords: Multifunctional material, structural battery, carbon-fiber composite, lithium-ion battery, mechano-electrical characterization

1. Introduction

Electric vehicles (EVs) promise to drive down petroleum consumption significantly, mitigate greenhouse gas emissions, and increase energy efficiency in transportation [1, 2]. Despite their compelling advantages, EV sales still represent only 1% of the 17 million US vehicles sold in 2017 because of factors including 'range anxiety', 'charging time trauma', and high purchase cost [3-6]. Unlike gasoline-powered cars, EV battery pack weight is a significant portion of the total vehicle weight, which is directly correlated with the vehicle's driving range limitations and high purchase cost [7, 8]. Research approaches to EV battery enhancement have thus primarily focused on improving battery chemistry and cell-level energy density, particularly for high-energy lithium-ion (Li-ion) batteries [9-11]. This represents the industry's current development strategy to reduce the energy-to-weight ratio, improve the range and performance, and reduce the cost of EVs [5, 12, 13]. However, there is an inherent trade-off in this approach, in that high-specific-energy batteries are often susceptible to mechanical intrusion and deformation, along with thermal runaway [14]. Typical battery packs are therefore compounded by layer upon layer of vehicle-level mechanical enclosures and protection systems to guard the cells and provide mechanical stability while maintaining intimate contact between the functional components [7, 8, 14-16]. These overhead

components significantly reduce both the packing factor and the system-level energy density. For example, in state-of-the-art EVs, the weight and volume of the complete energy storage 'system', including protection systems and enclosures, can be as much as twice those of the cells alone [7, 8]. Additionally, the advantages of high-energy cells are also largely offset by the complexity and cost of the more demanding system-level engineering requirements [8].

Rather than the continuous and incremental cell-level improvement approach, this paper presents a disruptive, accelerated path to maximize EV battery performance and efficiency at the vehicle level (Figure 1). We use the system opportunities that arise when traditionally separate functions are combined by drawing from the scientific principles of disparate fields that do not typically intersect: electrochemistry and structural mechanics. This work introduces a novel form for structurally-integrated batteries called multifunctional energy storage composite (MESC) structures. MESCs constitute multifunctional energy-storage materials that are designed with sufficient intrinsic robustness and safety to ensure that external reinforcements are no longer required. The proposed material integration process allows the existing state-of-the-art battery materials, i.e., Li-ion batteries, to be encapsulated directly in structural materials such as high-strength carbon-fiber composites. Most importantly, the MESC construction uses interlocking polymer 'rivets' that are carefully positioned within the cell to secure the battery electrode layers in place (Figure 2). Akin to stabilizing a loose deck of cards, the rivet structures prevent the typical shear movement of the battery layers, thus allowing their inherent mechanical properties to contribute directly to the structure's load-bearing performance. As a result, they can be used as structural components in the EV chassis or frame, or as mechanical impact absorbers in the crumple zone. These capabilities may enable elimination of unifunctional protective components and vehicle structures, thereby dramatically improving vehicle performance and efficiency through system-level weight and volume savings. The use

of MESCs as energy-storage structures not only eliminates the need for unifunctional components but also provides tremendous flexibility in system design and de-centralization of the energy storage units.

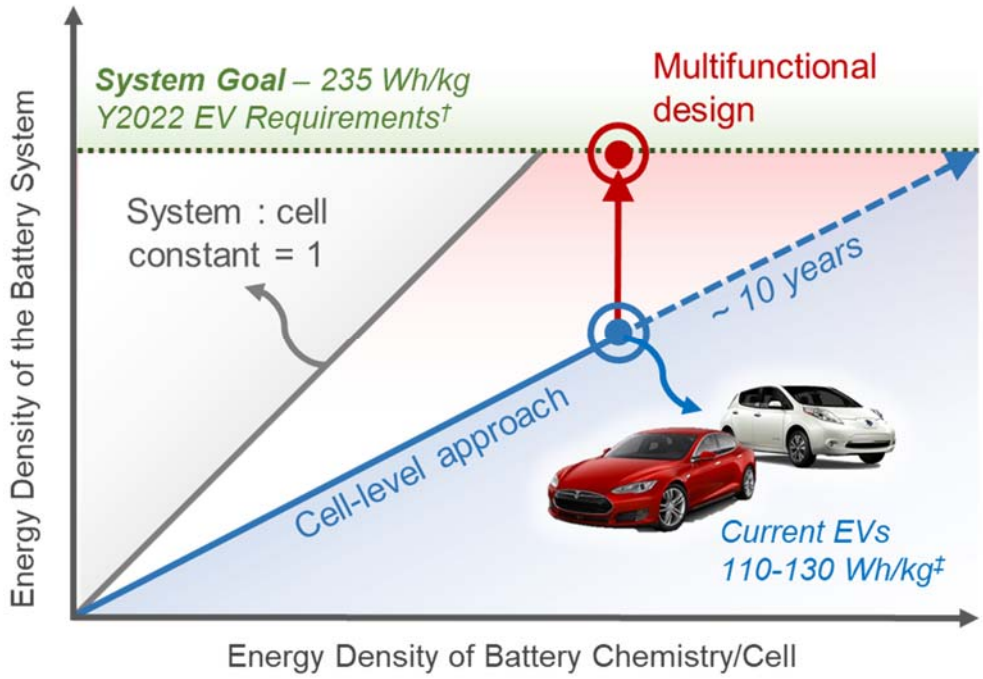

Figure 1. Development trends towards economically-viable EVs (adapted from [17]). †The US DOE and the US Advanced Battery Consortium (USABC) estimate that a specific energy target of 235 Wh/kg at the pack level will enable long-range, high-performance, and affordable EVs for widespread market adoption [8]. Current research approaches will require an extended period to reach this system goal because they are focused on improving the energy density of the battery cells/chemistry. High-energy cells require additional enclosures and support systems, which reduce the system-level energy density. System-level opportunities arise through multifunctional design of structurally-integrated batteries that can simultaneously serve as vehicle structural members and energy storage units. (‡ [7, 8].)

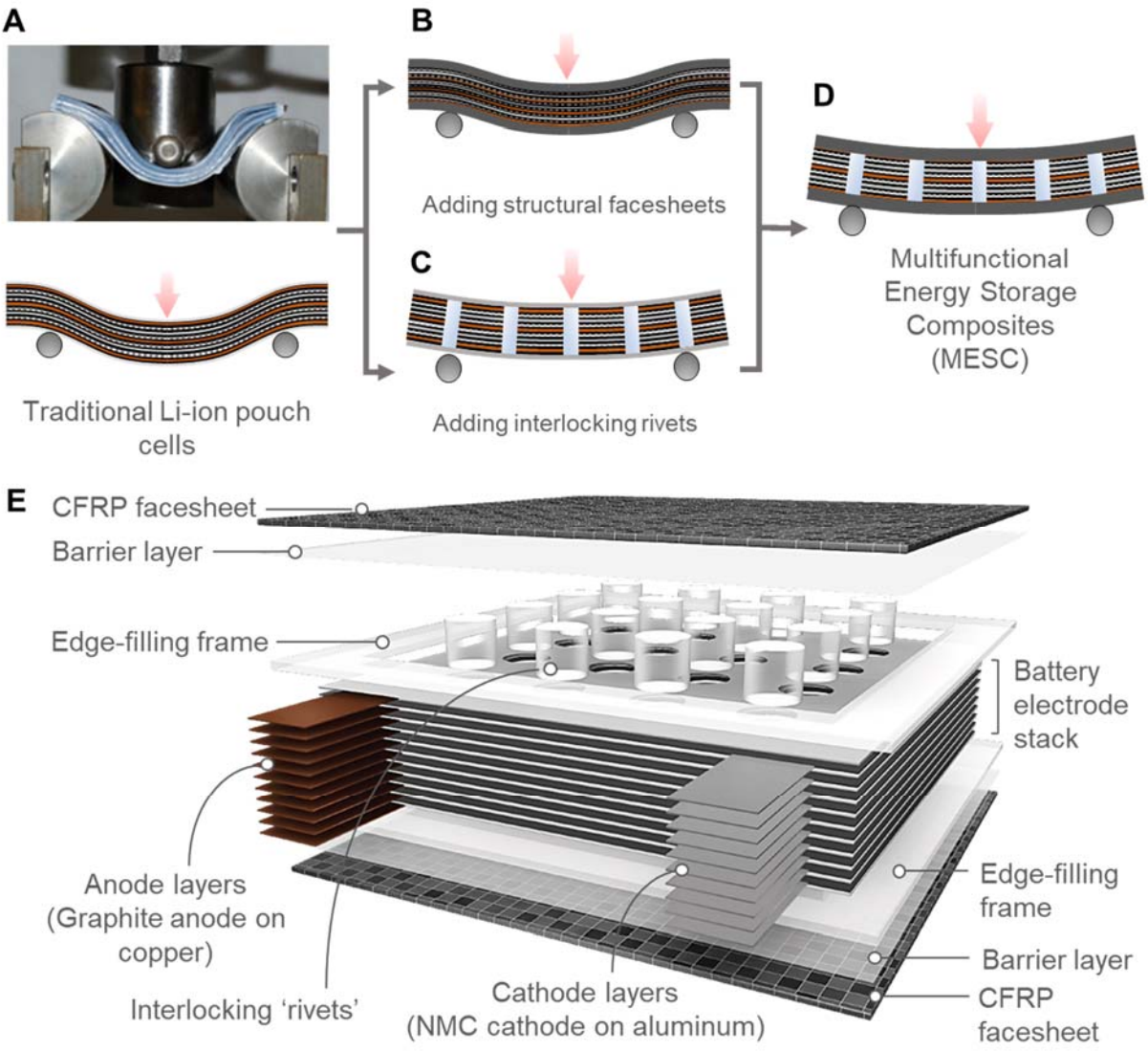

Figure 2. A-D) Mechanical comparison between MESC and typical Li-ion pouch cell. A) Pouch cells consist of loosely-laminated, thin electrode layers that provide minimal resistance to mechanical loading, similar to a loose deck of cards (Reprinted from [18], Copyright (2018), with permission from Elsevier); **B)** and **C)** show intermediate steps to enhance the structural robustness of Li-ion cells by addition of structural facesheets and interlocking rivets as separate solutions; **D)** MESCs use through-thickness rivets to interlock the sandwiched battery stack. These rivets inhibit shear movement of the layers while enabling load transfer through the core. The battery can thus contribute to the mechanical load-carrying performance. **E) 3D schematic illustration of MESC.** An array of through-thickness rivets is used to interlock a stack

of typical Li-ion battery electrodes three-dimensionally. These rivets are securely anchored on the encapsulating carbon-fiber-reinforced-polymer (CFRP) facesheets, allowing the entire unit to act as a mechanically-efficient sandwich structure.

The multifunctional structural battery concept became an area of research interest almost two decades ago, with limited initial success [19-22]. However, researchers have since had further opportunities for advanced development of structurally integrated batteries (and capacitors and supercapacitors) following recent developments in tangentially-related technology fields, including material synthesis, characterization techniques, and computational modeling [22-40]. The first group of efforts represented a holistic, top-down approach that aimed for shape, packaging, and load path optimization of off-the-shelf batteries. Approaches ranged from optimization of the directional arrangements of batteries to enhance their structural stability [22, 30, 41] to encasement of pre-packaged batteries in lightweight structural materials [19, 25, 26, 31, 32, 42, 43], and ingenious load path redirection techniques for improved crash absorption [35, 44]. At a more fundamental material level, the second bottom-up approach aimed to modify the compositions or structures of the battery materials to enhance their mechanical robustness. This approach is exemplified by numerous research efforts that include the introduction of structurally-enhanced polymeric or ceramic electrolytes [38-40, 45-47], fiber- or particle-reinforced electrolytes and binder materials for the electrodes [23, 48, 49], novel structural materials with intercalation properties [24, 27, 34, 50, 51], and synthesis of energy storage materials in strong fibrous forms [36, 52]. While many impressive results have been achieved in both cases, the intrinsic structural capabilities of the existing internal cell components are harnessed only marginally. While the top-down approach can be used for rapid realization of structural battery systems that are almost application-ready, it falls short because of a lack of synergy between the disparate and unifunctional subcomponents. The bottom-up approach is more

transformational but requires a tremendous effort to scale up for practical use and also suffers from a drastic trade-off between the energy storage capabilities that must be sacrificed and the mechanical improvement recovered. As a result, the multifunctional structural battery concept has been a risky and unsolved development challenge until very recently.

1.1 Problem Statement

State-of-the-art pouch Li-ion batteries are primarily designed for maximum energy storage performance; as a result, their mechanical load-carrying capabilities and robustness are minimal. Li-ion pouch cells are fundamentally constructed using a stack of alternating anode and cathode layers that are separated using thin micro-porous polymer separator membranes (Figure 2A). The individual paper-thin electrode sheets are composed of excellent structural materials such as copper and aluminum current collectors but are loosely stacked. Therefore, mechanical coupling and load transfer do not occur between these layers [18, 20, 43, 53]. In a manner similar to bending of a thick book, exertion of the slightest mechanical load on a battery can cause excessive deformation and relative slippage between the layers. Additionally, the electrode stack is generally packaged in a vacuum-sealed aluminum-polymer-laminate packaging material that offers minimal mechanical protection. Therefore, a strategy that can synergistically use the intrinsic load-bearing performances of existing internal battery components to build mechanical robustness directly into these cells would offer tremendous potential savings in both weight and volume.

1.2 Approach

This work thus introduces MESC structures as an alternate strategy towards fabrication of structural load-bearing batteries – an intermediate, multidisciplinary strategy. MESCs represent a novel form of

multifunctional structural battery materials that can carry mechanical loads while simultaneously providing energy-storage capabilities (Figure 2). MESCs provide a disruptive integration technique that allows high-energy Li-ion battery electrode materials to be embedded in high-strength carbon-fiber-reinforced-polymer (CFRP) composites. The novelty of MESCs lies in their incorporation of through-thickness interlocking polymer 'rivets' that extend through carefully designed perforations in the battery stack to interlock the electrode layers and securely anchor these layers onto the structural CFRP facesheets (Figure 2D). Standard industry electrodes can be adapted to function directly within this design without any requirement for battery chemistry modifications, which may be crucial for industry adoption.

Like sandwich structures, the comparatively stiff CFRP facesheets are placed on either side of the electrode stack, separated by the electrode core thickness, to carry the majority of the bending moment [54, 55] (Figure 2B). This sandwich-style construction effectively increases the moment of inertia of the laminate, giving it higher flexural rigidity. However, without the interlayer shear resistance of the battery core, the thin battery layers tend to bend around their own individual neutral axis, and the structural contributions of the facesheets will be minimized. The interlocking rivets therefore act to inhibit interlaminar slippage between electrode layers, thus allowing effective transfer of the shear stress through the battery stack to the CFRP facesheets (Figure 2C). This is analogous to use of stud shear connectors in civil construction to enhance the shear interaction and the load transfer between concrete and steel sections [56-58]. The shear transfer allows the battery laminate to bend around a common neutral axis, thus using the intrinsic mechanical properties of the electrode layers efficiently and making them a suitable sandwich structure core material.

The final MESC configuration is dependent on the actual intended application because MESCs can be tailored to meet specific mechanical (e.g., stiffness, strength) and electrical (e.g., gravimetric and/or volumetric energy densities) requirements. This work focuses on a proof-of-concept design and

fabrication of a Li-ion battery MESC. The first-generation MESC cells undergo a series of mechano-electrical tests, where emphasis is placed on quantification of the cell electrochemical and mechanical properties to assess performance of MESCs as load-bearing energy storage units.

2. MESC Design and Fabrication

2.1 Design Space

The design and analysis of the MESC represent a material optimization problem, where the material selections and geometric configurations allow a myriad range of possible mechanical-electrical performance combinations. When the MESCs are considered as typical sandwich structures, the most fundamental metric of their mechanical load carrying performance is the material compliance to deformation under a three-point bending load (Figure 2D), which, per unit width, follows the expression:

$$\frac{\delta}{P} = \left(\frac{L^3}{48}\right)\frac{2}{E_f t c^2} + \left(\frac{L}{4}\right)\frac{1}{G_c^* c} = \left(\frac{L^3}{48}\right)\frac{1}{D_{eff}} \qquad (1)$$

$$\downarrow \qquad \downarrow$$

$$1/D_f \qquad 1/U$$

where δ is the deflection of the sandwich beam under a load P. The terms in parentheses are constants that are specific to the loading conditions, and L is the length between loading supports. D_f is the flexural rigidity contribution of the stiff facesheets and U is the effective shear rigidity of the core. These rigidity parameters are dependent on the material properties and geometric configurations of both the facesheets and the core, where E_f is the Young's modulus of the facesheets, G_c^* is the effective shear modulus of the

core, and t and c are the thicknesses of the facesheets and the core, respectively. The combined rigidity effects result in the effective flexural rigidity of the composite sandwich structure, D_{eff}.

The rivets in the MESC enhance G_c^* by interlocking the electrode layers and thus inhibiting shear movement of the electrode stack. When interlocked, the electrode layers can contribute their intrinsic mechanical properties to the structural load carrying performance of the structure. The degree of mechanical interlocking is heavily dependent on the size, density, and distribution of the rivets, along with their material properties. These parameters simultaneously govern the apparent volume of the active battery, which defines the gravimetric and volumetric energy densities of the MESC. Determination of an optimal rivet topology in conjunction with the facesheet and core thicknesses and the facesheet material represents an interesting research problem in itself and will be discussed in detail in a companion publication.

2.2 Fabrication

In this work, the configuration was fixed and we considered an MESC with square electrodes and square grids composed of circular rivets (Figure 2E) to validate the feasibility of the concept and evaluate both manufacturability and cell performance. An MESC single cell (Figure 2) represents an MESC in its simplest form. An MESC cell is composed of the following three main components: i) the core battery electrode stack; ii) the structural facesheets; and iii) the reinforcement rivets. The step-by-step MESC cell fabrication process is illustrated in Figure 3.

First, the *battery core* is constructed using a stack of Li-ion battery anode and cathode layers arranged in alternating fashion and separated using polyolefin separator layers (Figure 3A). Before lamination, the electrodes are cut and perforated at pre-defined locations for the through-thickness rivets. In this work, the cathode and the anode were composed of conventional production-active materials, which were

lithium nickel-manganese-cobalt oxide (NMC) on aluminum foil and graphite on copper foil, respectively (Farasis Energy, Inc.). All sample types used 11 anode and 10 cathode layers with external electrode dimensions of 90 mm × 90 mm (as measured on the anode). The perforation patterns were square grids of equally-spaced 5-mm-diameter holes. A separate cathode design was produced such that the anode coverage is slightly larger than that of the cathode (0.5 mm in every direction, including perforations) to ensure that excess anode material was present and reduce the possibility of shorting. After stacking, the separators were spot-melted using 4 mm diameter heated rods to bridge the through-thickness holes. The cathode's copper current collectors were welded together ultrasonically onto a nickel tab, while the anode's aluminum current collectors were welded onto an aluminum tab. The complete electrode stack had a measured thickness of approximately 3 mm.

Figure 3B shows the fabrication of the *structural facesheets*, which consist of a structural layer that is passivated using a thin barrier layer made from the same thermoplastic material as the rivets. This barrier layer allows the rivets to be bonded securely to the facesheets while simultaneously acting as an encapsulation layer for the electrochemical cell. The structural layer and the barrier layer were fabricated separately before the passivation step. CFRP composites were used as structural layers here because of their excellent strength/stiffness-to-weight ratio. Dry 3K 2x2-Twill T300 carbon fiber fabric (Toray) was used to fabricate the CFRP composites in a vacuum-assisted resin infusion process. Three carbon fiber layers ([0°, 90°] orientations) with total thickness of 0.8 mm were infused with an unmodified liquid epoxy system (Bisphenol A diglycidyl ether + triethylene tetramine (stoichiometric); Sigma-Aldrich). The resulting laminate was then cured at room temperature for 24 h, followed by a post-cure at 90°C for 30 min. Polyethylene-co-acrylic-acid (EAA) ionomer thermoplastic (Dupont) in pellet form was compression molded into a 150 μm-thick sheet to form a barrier layer. This barrier layer was then bonded to the surface of the structural facesheet via vacuum-assisted compression at 150°C for 30 min.

The *MESC assembly and riveting* process is illustrated in Figure 3C. Cylindrical injection-molded EAA rivets (4 mm diameter) were inserted into the perforations within the electrode stack. The battery stack was then placed in the opening between two half-thickness edge-filling frames (110 mm × 110 mm, 1.5 mm thickness, with a 90 mm × 90 mm opening), which enclose the liquid electrolyte within the electrode stack. The battery core was then sandwiched between two facesheets, with the barrier layer facing inwards. The resulting laminate was compression molded in a heated hydraulic press to melt and fuse the polymer rivets securely to the structural facesheets (100°C, 0.5 MPa pressure). The laminate was then allowed to cool under pressure to room temperature; during this period, the polymer solidified and thus mechanically stabilized the electrode stack.

During the compression molding process, a through channel was also molded into one of the cell edges for *electrolyte filling* (Figure 3D). The MESC cells were filled using a standard lithium-salt liquid electrolyte ($LiPF_6$ in EC/DMC/ DEC organic solvent, 10 mL (Farasis Energy, Inc.)) through the prepared channel in a similar manner to the conventional pouch cell process. The channel was then sealed, and the cells went through a standard solid-electrolyte-interface (SEI) formation process. The channel was then re-opened to allow degassing and was cut and resealed locally at the edge-filling frame.

Four sample types were fabricated, as detailed in Table 1. All four sample types shared the same electrode footprint (90 mm × 90 mm, measured on the anode (Figure S1, Supplementary Information)) and the same number of electrode layers (21 layers, ~3 mm thick) to enable fair electrochemical comparison. *Baseline Pouch* cells were constructed to act as electrochemical control structures in which the nonperforated electrode stacks were packaged directly in typical aluminum-polymer-laminate pouches (Figure S2, Supplementary Information). As the mechanical benchmark, *CFRP/No Rivet* cells were constructed by encapsulating nonperforated battery stacks without rivets inside CFRP (three plies of 3K woven CFRP, approximately 1 mm thick). These *CFRP/No Rivet* cells emphasized the beneficial

mechanical contributions of the rivets and isolated the inherent electrochemical impact of the perforations from CFRP encapsulation. Two types of MESC cells (*MESC 4×4* and *MESC 5×5*) were constructed using different rivet topologies to study the effects of rivet density on the electrochemical and mechanical performance. The *MESC 4×4* and *MESC 5×5* cells contained four-by-four and five-by-five arrays of equally spaced 5-mm-diameter rivets, respectively.

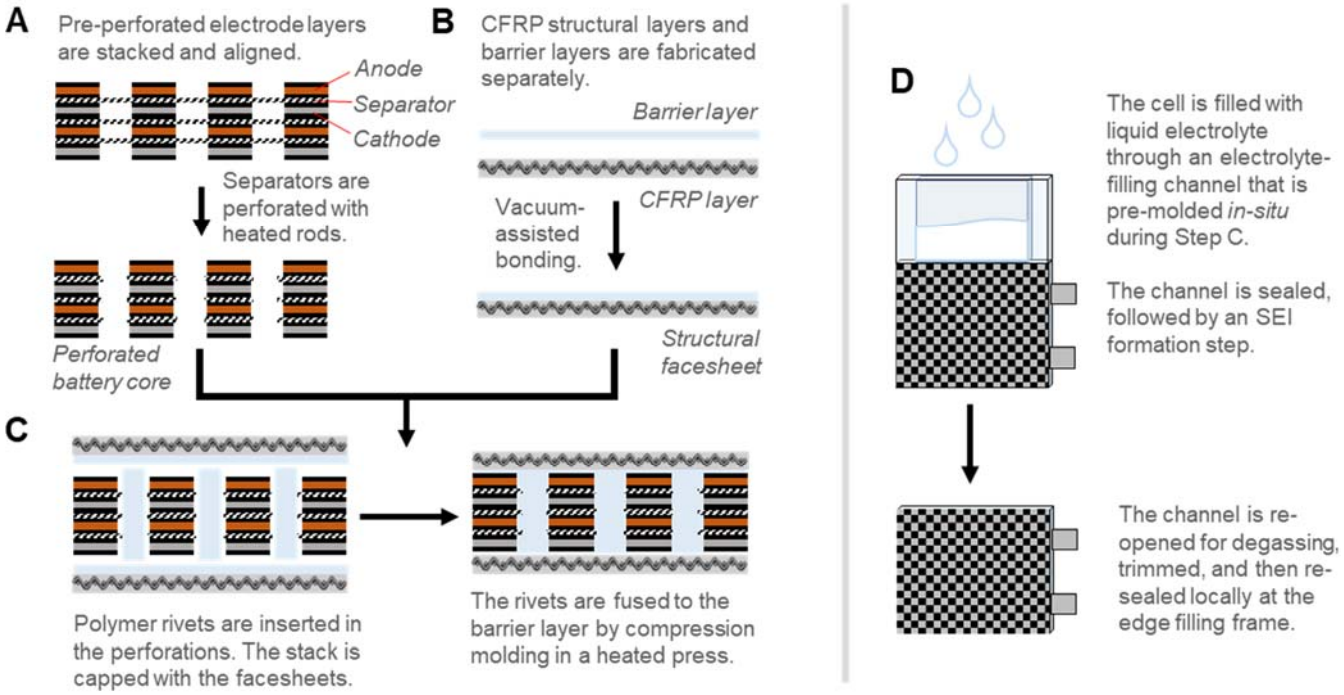

Figure 3. MESC fabrication process. A) Perforated anode/cathode layers are laminated in alternating fashion, followed by local heating of the separator layers to create through-holes; **B)** structural facesheets are fabricated by vacuum-assisted bonding of CFRP plates and thin EAA barrier layers; **C**) the MESC assembly and riveting process uses compression molding to melt and fuse rivets to the encapsulating facesheets; **D)** the cell is filled with liquid electrolyte through a pre-formed channel. The cell is then sealed, formed, degassed, and resealed.

Table 1. Sample description

Sample type	Sample description	Dimensions and weight	Active surface area per layer and theoretical capacity
Baseline Pouch	Nonperforated battery in aluminum-laminate pouch	90 mm × 90 mm × 3.5 mm 81±1 g	7,921 mm^2; 4,602 mAh (100%)
CFRP/ No Rivet	Nonperforated battery in CFRP but without rivets	110 mm × 110 mm × 5 mm 120±5 g	7,921 mm^2; 4,602 mAh (100%)
MESC 4×4	MESC with 4×4 perforation array	110 mm × 110 mm × 5 mm 120±5 g	7,469 mm^2; 4,340 mAh (94.3%)
MESC 5×5	MESC with 5×5 perforation array	110 mm × 110 mm × 5 mm 120±5 g	7,215 mm^2; 4,192 mAh (91.1%)

3. Experimental Methods

3.1 Electrochemical Characterization

After the SEI formation process, the samples were subjected to an initial slow-rate calibration cycle between 3.0 V and 4.2 V to obtain the C-rate, or the current rate at which the battery is discharged in 1 h. The cells then underwent the initial electrochemical reference performance test (RPT). At the beginning of life (BoL) of each sample, the initial discharge capacity of each sample was quantified during constant current (CC) cycling at a C/10 current rate, or approximately 400 mA (1C = 4,000 mA). The initial C/10 discharge capacity determined the apparent (measured) capacity of the cells for comparison to the expected capacity that was calculated based on the amounts of active materials added. As a rate capability indicator, the cell's DC impedance at the BoL was measured using a hybrid pulse power characterization (HPPC) test profile (Figure S6, Supplementary Information) [59]. The technique was used to evaluate the cell's DC impedance at every 10% of the depth of discharge (DoD) by measuring the voltage difference during current interruption. The cells were then cycled using a C/3 CC profile, or at approximately 1,300

mA. The C/3 charge-discharge cycle was repeated to evaluate the cell life cycle performance by comparing the discharge capacity retention properties with increasing numbers of cycles of the different sample types. All electrochemical testing was performed at a constant 30°C in a low-temperature oven. The batteries were cycled using Landt CT2001 battery analyzers (Landt Instruments), except during the HPPC test, which was performed using a high-current Arbin BT2000 battery tester (Arbin Instruments).

3.2 Quasi-Static Three-Point Bending

The quasi-static mechanical testing was performed using a three-point-bending fixture with a cylindrical-roller load applicator and supports on a mechanical test machine (100 kN servo-hydraulic load frame, MTS Systems Corporation) (Figure S7, Supplementary Information) [60, 61]. A vertical downward force was applied from the top using the cylindrical load applicator along the line at the mid-span. The interlayer-shear inhibition capabilities of the through-thickness reinforcements were validated by measuring and comparing the sample's effective flexural rigidity (D_{eff}), which is the resistance of the structural member to bending deformation. The load was applied at a constant displacement rate of 3.33 mm/min (quasi-static). The vertical displacement at mid-span was measured constantly throughout the experiment using a linear variable differential transducer. The load was applied quasi-statically and the test was interrupted when the mid-span deflection reached 1 mm. The displacement was then held constant while an in-situ electrochemical RPT was performed (a C/3 cycle, followed by DC impedance measurements via current interruption using an HPPC profile). The RPT was then repeated for a 2 mm mid-span deflection.

3.3 Cyclic Three-Point Bending (Mechanical Fatigue)

The three-point-bending test setup used in the quasi-static experiment was used again here. In this case, the mid-span load was applied repeatedly in a cyclic manner (to produce mechanical fatigue), with a peak load of 700 N. (This peak load is approximately 80% of the static failure load for the *CFRP/No Rivet* cells. Because of their higher effective bending rigidities, the peak load is equivalent to approximately 20% of the static failure loads of the *MESC 4×4* and *MESC 5×5* coupons.) The loading ratio was chosen to be R=0.3, which resulted in a mean load of 450 N and a minimum load of 200 N. The cyclic load has a sinusoidal profile with a frequency of 0.3 Hz. Before each load application segment, all samples were pre-conditioned to adjust their open-circuit voltages to 3.8 V using a C/5 constant-current constant-voltage charge profile with a C/20 cut-off current. Mechanical loading was stopped every 100 cycles. The samples were then unloaded and removed from the mechanical test machine. Sequential electrochemical characterization (C/3 cycling and HPPC testing, repeated three times to obtain an average) was performed at a constant 30°C inside an environmental chamber. After the 3.8 V constant-current/constant-voltage conditioning, the tests were then repeated for another 100 cycles up to a maximum 1,000 cycles. The test flowchart is shown in detail in Figure S8 (Supplementary Information). The discharge capacity retention and the DC impedance under increasing numbers of mechanical cycles were compared to evaluate any nonfatal electrochemical performance degradation caused by mechanical fatigue.

4. Results and Discussion

4.1 Electrochemical Performance

The MESCs require thorough electrochemical characterization because their construction differs significantly from that of conventional Li-ion cells. Their electrical functionalities must be compared with those of the *Baseline Pouch* cells from an end application viewpoint in terms of apparent cell capacity, cell DC impedance, and, most importantly, the life-cycle performance. The electrochemical results for all sample types are presented in Figure 4B–E. Figure 4B shows the cell voltage time-histories for nominal C/10 cycles of a representative *MESC 4×4* cell and a *Baseline Pouch* cell, illustrating that the typical inherent graphite/NMC chemistry characteristics are maintained.

Apparent Capacity. Figure 4C shows the apparent first discharge capacities (C/10) of the *Baseline Pouch*, *CFRP/No Rivet*, *MESC 4×4*, and *MESC 5×5* cells in comparison with their corresponding theoretically determined values. The theoretical capacity for each cell type was calculated using the active material loading multiplied by the surface area remaining after perforation, as listed in detail in Table 1. The active surface area of the *MESC 4×4* cells was 94.3% of that of the unperforated baseline (i.e., *Baseline Pouch* and *CFRP/No Rivet*) cells because of the four-by-four perforations, while the corresponding figure was 91.1% in the *MESC 5×5* case. As a result, the theoretical first discharge capacity also decreased as the area loss due to the perforations increased in the *MESC 4×4* and *MESC 5×5* cells (see Table 1, Theoretical capacity).

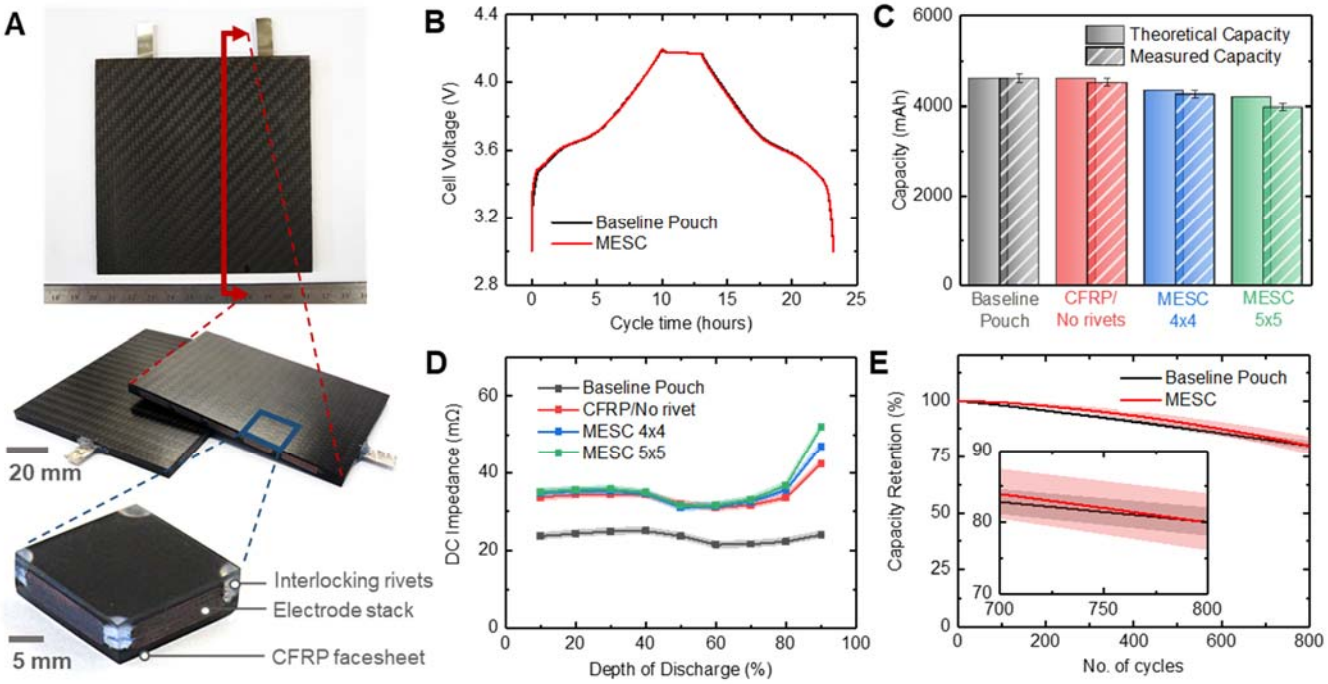

Figure 4. A) As-fabricated MESC coupon. The cross-sectional view shows the MESC's internal components: the perforated battery core, rivets, CFRP facesheets, and edge-filling frame. The building-block unit cell, with the CFRP replaced by translucent glass-fiber composites, shows the battery stack being constrained by rivets at each corner. **B-E) Electrochemical results. B)** Charge-discharge voltage curves, where the *MESC* cells show the unaltered and inherent graphite/NMC chemistry characteristics similar to those of a *Baseline Pouch* cell; **C)** apparent capacity, where the MESC's apparent capacity is reduced only very slightly because of its construction as compared with its theoretical capacity; **D)** DC impedance, where a considerable increase in DC impedance suggests that further development is required on the cell design and fabrication process; **E)** capacity retention, where the MESC shows excellent capacity retention (80% retention at 800 cycles) similar to that of *Baseline Pouch* cells. The error bars and shaded areas in C–E) represent the standard deviations of five replicated samples.

The apparent first discharge capacities of the *MESC* and *CFRP/No Rivet* cells were marginally lower than the corresponding theoretical values (4,510 mAh [−2.0% from theoretical value] for *CFRP/No Rivet* cells, and 4,243 mAh [−2.3%] for the *MESC 4×4* and 3,974 mAh [−5.2%] for the *MESC 5×5*). These drops in capacity were likely to be caused by the nonstandard cell fabrication process and imperfections associated with the perforations. The high-temperature, high-pressure cell fabrication process may cause the electrode layers and separator to deform or wrinkle slightly, which then impairs the ionic pathway. The presence of the facesheet and the polymer reinforcement materials could also affect the electrochemistry and thus affect cell capacity. Therefore, despite having nonperforated structures, the *CFRP/No Rivet* cells still see a small 2.0% discrepancy that can be improved through process optimization.

Additionally, the perforated electrodes in the *MESC 4×4* and particularly in the *MESC 5×5* have more free edges (i.e., around the holes) than their nonperforated counterparts. Imperfections from the electrode cutting processes, such as edge burrs and active material flaking, would be more pronounced for the perforated electrodes. Slight misalignments between adjacent anode-cathode pairs could also reduce the apparent active surface area, leading to reduced cell capacity. While a slightly larger discrepancy was seen in the *MESC 5×5*, the *MESC 4×4* sample could still produce a similar performance to the nonperforated *CFRP/No Rivet* baseline. Moreover, the *MESCs* are currently designed with a generous 1-mm anode overhang to prevent lithium plating, shorting, and safety issues if the electrodes are slightly misaligned owing to the nonmechanized nature of the current fabrication process. The overhang regions accept lithium ions during the slow formation process which also dwells at high SoC for a prolonged period of time [62, 63]. The ions might be trapped in the overhang portions during the subsequent discharge process making the discharge capacity lower. As the MESC manufacturing process becomes more mature with better electrode alignment, the extent of anode overhang may be reduced which further improves the apparent capacity delivery.

Energy Density. The gravimetric and volumetric energy densities can be calculated by multiplying the apparent cell capacity by the nominal cell voltage of 3.7 V and then normalizing with respect to the cell weight or volume. The gravimetric energy densities of the *Baseline Pouch*, *CFRP/No Rivet*, *MESC 4×4*, and *MESC 5×5* samples are 210, 139, 131, and 123 Wh/kg, respectively, while the corresponding volumetric energy densities are 601 Wh/L, 276 Wh/L, 260 Wh/L, and 243 Wh/L. To put this into perspective, the gravimetric energy density of the first-generation *MESC 4×4* structurally-integrated battery was 62% of that of the unifunctional *Baseline Pouch* cell, while its volumetric energy density was 43% of that of the *Baseline Pouch* cell.

The drop-in energy density is dependent on the proportion of non-energy-storing parts in the MESC (e.g., CFRP facesheets, edge-filling frames, and rivets). This is primarily governed by the ratio of the facesheet thickness to the electrode stack thickness, among many other parameters. Without access to an automated electrode stacking system, which is widely used in the battery industry, the bottleneck in the in-house fabrication process was fabrication of the precisely-aligned electrode stacks. The moderate stack thickness was selected to ensure that we obtained sufficient numbers of replicate samples for each experiment. Simple calculations show that by doubling the electrode stack thickness while maintaining the facesheet thickness, energy densities of up to approximately 150 Wh/kg and 310 Wh/L could be reached, with 160 Wh/kg and 330 Wh/L produced by tripling the stack thickness. This also represents an opportunity for design trade-offs over the entire implementation space.

DC Impedance. Figure 4D shows the DC impedances of the four cell types at the BoL as a function of the DoD, as calculated from current interruptions during an HPPC test profile. All cell types showed the inherently convex characteristics of the graphite/NMC chemistry. However, all cells that underwent the CFRP encapsulation process (i.e., *CFRP/No Rivet, MESC 4×4*, and *MESC 5×5)* had higher DC impedances (~40% higher at low DoD) than the *Baseline Pouch* cell. This increased impedance was

stronger towards the end of the discharge (higher DoD). Similar to the apparent capacity, this effect on the DC impedance was attributed to the nonstandard, high-temperature, and high-pressure cell fabrication process, which still has room for improvement. For example, the process conditions could be fine-tuned to minimize pore closure in the separator. Additionally, use of the structurally stronger encapsulation rather than the traditional vacuum-assisted diffusion process means that electrolyte wetting may be improved by injecting the electrolyte using positive pressure.

The effects of the added perforations on the increased impedance were found to be very subtle for large parts of the DoD. A noticeable impedance increase (>10%) could only be seen within a small range of high DoD (>80% DoD) in the *MESC 4×4* and *MESC 5×5* samples, with the former performing better than the latter, as expected. The perforations were believed to cause local spreading and constriction of the current flow and a nonuniform current density distribution, which led to increased impedance. However, the results here showed that the effect on the DC impedance was moderate and only manifested at a high DoD when the current density distribution was most nonuniform. The MESC current density distribution is worthy of thorough future study to enable optimized rivet placement and minimize placement impact on the impedance, thermal performance, and power capabilities.

Life Cycle Performance. Figure 4E shows the MESC's life cycle performance as compared with the baseline chemistry. Capacity retention after repeated C/3 cycling is shown as a function of the cycle number. The capacity retention of the *Baseline Pouch* cell, plotted here in black, represents the expected life cycle performance of the baseline chemistry in the as-fabricated form factor. No discernable differences were observed among the capacity retentions of the *MESC 4×4*, *MESC 5×5*, and *CFRP/No Rivet* cells; their data are thus plotted together as '*MESC*' in red. Interestingly, all cell types were able to retain 80% of their original capacities after 800 cycles (0.025% per cycle). Despite the novel cell structure and fabrication technique, *MESC* can maintain a similar life cycle performance to that of industry-standard

pouch cells with the same chemistry. Although small discrepancies were observed in the slopes of the capacity retention curves between the *Baseline Pouch* and the *MESC*, they were mainly caused by slower electrolyte wetting in the *MESC* cells, which will be improved in future iterations. Furthermore, the aforementioned anode overhang effect may cause additional SEI to be formed on the overhang regions which consumes lithium. This issue will also be addressed by improving the electrode alignment and cell design in future studies.

In summary, our preliminary electrochemical characterization has demonstrated that functional *MESC* cells can be fabricated successfully with electrochemical capabilities that are comparable to those of conventional Li-ion batteries . Modifications to the cell architecture and the fabrication process will be made in subsequent iterations to optimize the cell performance, particularly in terms of apparent cell capacity, energy density, and DC impedance. More controlled fabrication is also required to minimize the cell-to-cell variations and improve reproducibility and reliability.

4.2 Performance During Quasi-Static Three-Point Bending

A quasi-static mechanical three-point bending test (Figure 5A) was performed on the cell samples to compare the mechanical performance of the MESC with that of the nonriveted cells and the conventional pouch cells. The MESC's electrochemical functionalities were also characterized while the cells simultaneously carried a sustained mechanical load. The mechanical and electrochemical performance results for these samples during quasi-static three-point bending are shown in Figure 5.

Flexural Rigidity. Figure 5A shows the load-displacement plots for all sample types under quasi-static three-point-bending loads. *Structural Sandwich* samples, which were formed using a solid EAA polymer core in place of the battery stack, were also measured in the experiments to represent the upper mechanical performance bound. The slope values $\frac{\delta}{P}$ were calculated via linear regression analysis of the load-

displacement data in the 0–0.5 mm displacement range. D_{eff} was then obtained using Equation (1), with calculated values of 0.7, 3.0, 11.0, 12.1, and 14.3 N·m^2 for the *Baseline Pouch*, *CFRP/No Rivet*, *MESC 4×4*, *MESC 5×5*, and *Structural Sandwich*, respectively. Note that the *Baseline Pouch* cells were tested over a shorter span and their D_{eff} values were adjusted as though they had the same area moment of inertia as the other sample types while assuming isotropic flexural behavior.

Comparison of the *Baseline Pouch* and *CFRP/No Rivet* cells shows that an improvement in D_{eff} was produced by simply encapsulating the battery stack in the CFRP facesheets, even without reinforcement rivets. However, these *CFRP/No Rivet* cells only saw minor increases in D_{eff} because their structural facesheets were not used at full efficiency, similar to observations in the literature [43]. Because relative shear movement still existed in these electrode layers, the shear stress could not be transferred readily through the battery stack core. As a result, the CFRP facesheets only carried the bending loads that were transferred through the edge-filling frame in the cell periphery.

In contrast, the additional four-fold increase in D_{eff} for the MESC cells when compared with the *CFRP/No Rivet* cells is particularly remarkable. This is more than fifteen times higher than that of the *Baseline Pouch* cells. It should also be noted that the *MESC 4×4* and *MESC 5×5* cells lost as little as 5.7% and 8.9% of their active material volumes for D_{eff} to be quadrupled when compared with the *CFRP/No Rivet* cells. With only a fraction of the battery volume being sacrificed, the *MESC*'s D_{eff} reached almost 85% of that of the *Structural Sandwich*, in which the entire battery volume was replaced with a structurally efficient polymer core. Having an equivalent construction to a typical sandwich structure, the *Structural Sandwich*'s D_{eff} represented an appropriate value for practical structural usage and the maximum mechanical limit for MESC construction.

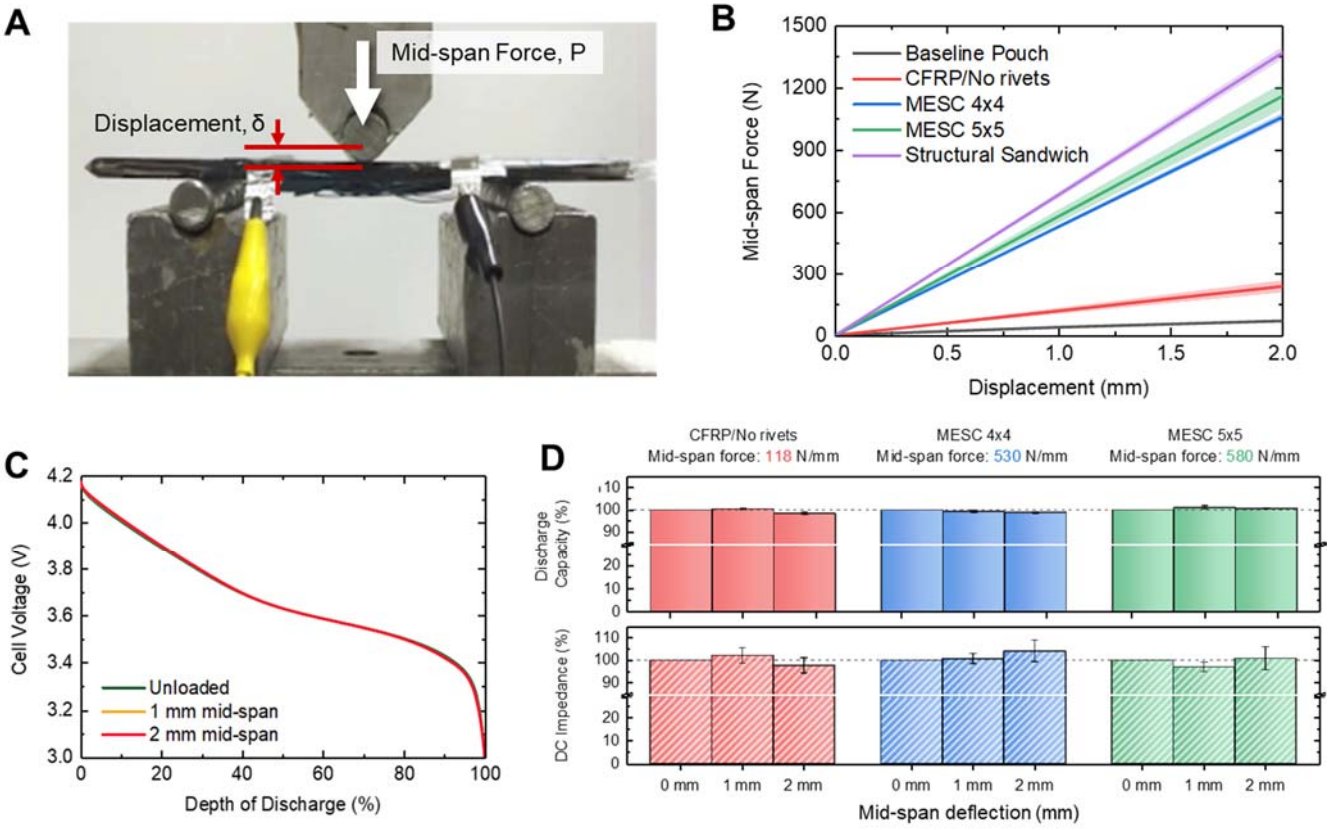

Figure 5. Mechano-electrical performance during quasi-static three-point bending. A) Experimental three-point bending setup; **B)** load-displacement plot, where the *MESC* shows significantly higher flexural rigidity D_{eff} than the *Baseline Pouch* cells. While the *CFRP/No rivets* cells are encapsulated in CFRP, the absence of rivets prevents effective load transfer through the core, leading to low D_{eff}; **C)** discharge curves from a typical *MESC 4×4* cell during constant-displacement bending, showing no discernable mechanical loading effects on continuous power delivery; **D)** effects of each mechanical loading increment on discharge capacity and DC impedance, showing that good electrical performance was maintained after cells were subjected to realistically large mechanical strain. The shaded areas in B) and error bars in D) represent the standard deviations of the five replicate samples.

The interlocking rivets efficiently eased shear stress transfer through the electrode stack to the CFRP facesheets. These rivets achieved this by reducing the characteristic bending lengths of the electrode layers while constraining their boundary conditions. This inhibited slipping motion in the electrode layers and established a continuous transverse shear stress, thus allowing the layered stack to bend around a common neutral axis. This allowed the CFRP facesheets to carry higher bending stresses, which led to significant improvements in D_{eff}. Higher CFRP utilization because of effective shear transfer was clearly observed from the normal bending strain in the *MESC* being larger than that in its *CFRP/No Rivet* counterpart (Figure S3, Supplementary Information). When the loose electrode layers were secured by rivets, the battery stack was able to participate in carrying the transverse shear, analogous to the core material of a sandwich structure. As a result, higher forces were required to deform the MESC by the same amount because greater strain was required on the CFRP facesheets because of their increased bending resistance.

Expanding Design Space. D_{eff} is scale-dependent, i.e., the D_{eff} of a sandwich structure increases as the square of the distance of the facesheets from the neutral axis increases. The D_{eff} of the MESC can be improved significantly by increasing the battery core thickness with respect to the facesheet thickness, which simultaneously improves the cell energy density (Figure S10, Supplementary Information). Furthermore, the saturation of D_{eff} that occurs with increasing rivet density shows that the interlocking efficiency can only be increased up to a certain extent, beyond which the capacity-stiffness trade-off shows inflection. In other words, to achieve a given set of capacity and stiffness requirements, an optimal rivet configuration and optimal cell cross-sectional geometry must be designed to obtain the maximum capacity and/or stiffness. Additionally, the optimal rivet configuration may not be restricted to the rectangular arrays of circular rivets used in this study. In a broader sense, the configuration can also include irregular, nonuniform rivet distributions along with variations in the rivet shapes and sizes. For the various loading

conditions, cell geometries, and CFRP-to-battery thickness ratios, structural optimization becomes a highly challenging but interesting problem that will receive special attention in a companion publication.

Linear Elasticity. We also confirmed the strong nonlinear behavior in the load-displacement curves for the *Baseline Pouch* cells (Figure 5B and, in greater detail, Figure S4, Supplementary Information), similar to previous observations in the literature [18]. This nonlinearity manifested in the forms of permanent deformation after unloading and creep during prolonged load application. Pouch cells initially have a small resistance to mechanical deformation because of their vacuum-sealed packaging, which constrains shear motion between the layers to a certain degree. However, this resistance diminishes readily when the load level overcomes the restraining pouch and the friction between the layers, or when the load is applied over an extended period. Without appropriate inclusion of elastic mechanical constraints, these layers are not able to spring back and the deformation thus becomes permanent.

Unlike the pouch cells, the load-displacement relationships of the MESC, and even those of the *CFRP/No Rivet* cells, remained linear up to the first observable mechanical failure (Figure S4, Supplementary Information). These samples could also be loaded and unloaded repeatedly without permanent plastic deformation, which allowed evaluation of their long-term electrochemical responses under mechanical fatigue. The mechanical failure occurred around the 5–5.5 mm mid-span deflection point across the different CFRP-encapsulated sample types. This corresponded to loads of approximately 850 N, 2750 N, and 3000 N for the *CFRP/No Rivet, MESC 4×4*, and *MESC 5×5* cells, respectively (Figure S4, Supplementary Information). Failure initiation was accompanied by delamination of the bottom facesheet from the edge-filling polymer frame, followed by cracking in the bottom CFRP and a load drop. Loading was stopped immediately after this load drop to prevent excessive deformation of the electrode and as a safety precaution to prevent shorting and possible thermal runaway. In future work, the failure modes, plasticity, and strength envelopes of these new materials will be studied and quantified to establish

safety-centric design guidelines. This is not a trivial linear exercise because these failure mechanisms may involve expansive combinations of mechanical and electrical failures, which will necessitate testing under various loading conditions using a well-protected experimental setup.

Electrochemical Performance under Sustained Loading. The effects of a quasi-static mechanical bending load on electrochemical functionality were quantified using in-situ electrochemical RPT (C/3 cycling followed by HPPC). It should be noted that this procedure could not be performed on the *Baseline Pouch* cells because creep deformation occurred under continuous application of a constant load, which is a further indication of their poor mechanical properties. Figure 5C shows the cell voltage time-histories of a representative *MESC 4×4* cell under a C/3 discharge profile for various mechanical loading conditions. Electrochemically equivalent behavior was observed before loading (pristine, 0 N load), at the mid-span displacement of 1 mm (530 N load), and at a displacement of 2 mm (1,060 N load). Similar to the *MESC 4×4*, the *MESC 5×5* and *CFRP/No Rivet* cells also failed to show any discernable deviations in their discharge curves with increasing mechanical loading up to the 2 mm mid-span displacement.

The C/3 discharge capacity and the cell DC impedance (at 50% DoD) characteristics during exposure to incremental quasi-static loads are shown in Figure 5D. The results at each load increment are normalized as percentages, with values corresponding to the pristine condition (100%; leftmost column of each cluster). No observable trends were found in the capacity and DC impedance results with increasing loading up to the 2 mm deflection. Any changes in the nominal values were within the experimental error range and were mainly caused by changes in the ambient temperature while lengthy, in-situ mechano-electrical testing was performed outside an environmental chamber.

Under significant strain levels (deflection of up to 2 mm over a 100 mm span), all the CFRP-encapsulated cells maintained their electrochemical functionalities. Under the same deformation, however, we observed that the MESC cells could carry significantly higher loads than their *CFRP/No*

Rivet counterpart, and were almost as high as traditional sandwich structures. The best performing cell, *MESC 5×5*, carried as much as 1,160 N at the maximum 2 mm deflection in these experiments, as compared with the 236 N carried by the *CFRP/No Rivet* cell. This shows that use of the MESC's interlocking rivets in efficient sandwich construction helps to maintain the battery's integrity and electrical connections, thus preventing any nonfatal electrochemical injuries from occurring during mechanical loading. This long-term exposure to mechanical loads to allow for in-situ electrical cycling could not be handled by the nonreinforced *Baseline Pouch* cells because of their permanent creep deformation.

4.3 Performance under Cyclic Three-Point Bending (Mechanical Fatigue)

This section describes the mechanical fatigue testing that was conducted to evaluate the performance of the rivets in suppressing electrochemical degradation under application of repeated cyclic mechanical loading. The rivets' ability to suppress both cyclic strain and deformation due to mechanical fatigue confirm the feasibility of practical implementation of the MESC structural battery as an energy-storing structural component. Figure 6A and Supplementary Movie S1 (Supplementary Information) show an *MESC 4×4* cell during cyclic three-point bending under a maximum load of 700 N, where the cell's concurrent electrical functionality is demonstrated by powering a DC fan while maintaining the appropriate cell voltage throughout the experiment. Discharge capacity and DC impedance data were collected every 100 mechanical cycles up to 1,000 cycles, as shown in Figure 6B and C.

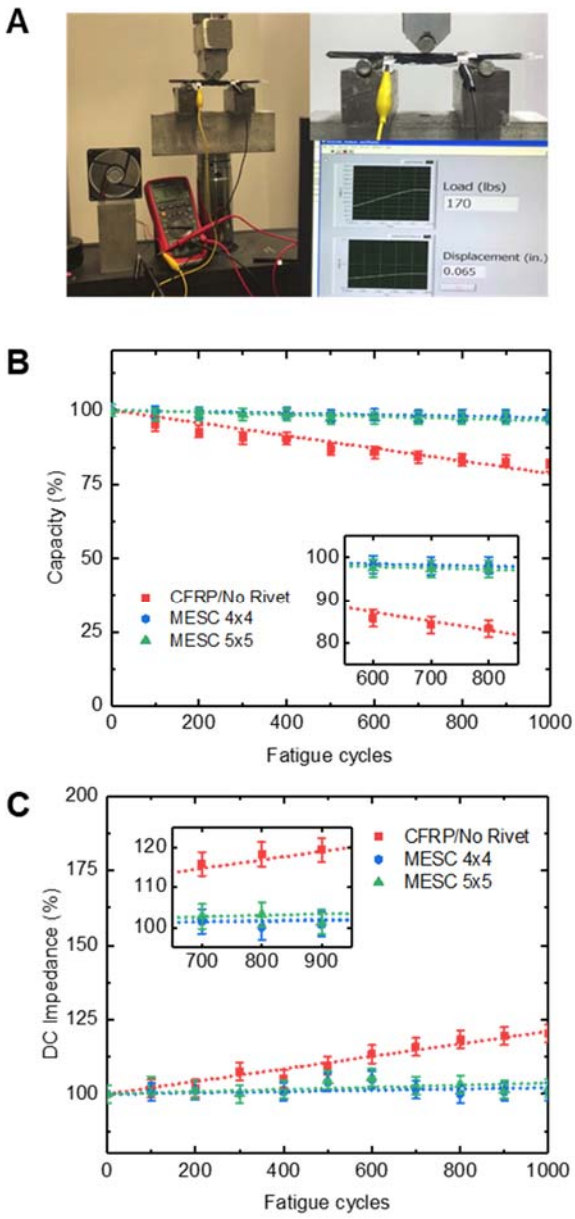

Figure 6. Electrochemical resistance to cyclic bending loading. A) *MESC 4×4* cell under cyclic bending loading between 200 and 700 N (50–200 lb), concurrently providing power to a DC fan while the terminal voltage is being measured; **B, C**) effects on discharge capacity and DC impedance, respectively, where the electrical performance remains almost unchanged for the *MESC* cells, while the *CFRP/No Rivet* cells suffer a significant capacity hit and increased impedance due to mechanically-induced electrical degradation. The error bars represent the standard deviations of five replicate samples.

Capacity Retention under Mechanical Fatigue. Figure 6B shows the C/3 discharge capacity retention characteristics versus the number of mechanical loading cycles. The discharge capacity results were normalized as percentages with respect to the values in pristine condition prior to the experiments. After 1,000 loading cycles, only approximately 79% of the first-discharge capacity was retained by the *CFRP/No Rivet* cells. However, the *MESC 4×4* and *MESC 5×5* cells showed 98% and 97% capacities, respectively. In contrast to the obvious 21% fading observed in the *CFRP/No Rivet* cells, the MESCs experienced only 2-3% capacity loss, which after subtracting the electrical cycling-induced fading, was well within experimental error (10 segments of 100 loading cycles involved more than thirty electrical RPT cycles which were estimated to cause ~1–1.5% capacity degradation themselves). To put this into perspective for the mechanical fatigue, the electrical degradation of the mechanically nonreinforced *CFRP/No Rivet* cell could be as high as 50 mechanical cycles per 1% capacity degradation, while the MESC could withstand *330–500 cycles per 1% degradation*. It should be emphasized again that the *Baseline Pouch* cells were excluded from this experiment because they experienced permanent deformation after the first load application.

This capacity fade was attributed to excessive cyclic strains from the repeated mechanical loading, similar to the electrical-cycling-induced mechanical strains. The nonreinforced *CFRP/No Rivet* cells experienced four times as much deformation and mechanical strain as the interlocked MESC cells because of their lack of mechanical load transfer and poor structural integrity. As a result, at the same peak load of 700 N, a larger maximum curvature of 4 mm over a 100 mm span was observed in the *CFRP/No Rivet* cells, as compared with 1 mm deflection in their stiffer MESC counterparts. The cyclic responses of the load, displacement, and maximum bending strain that were observed during the fatigue experiment are shown in Figure S5 (Supplementary Information). This higher cyclic deformation in the battery electrodes thus caused significantly faster fading in the nonriveted cells.

DC Impedance under Mechanical Fatigue. Figure 6C shows the normalized DC impedance (at 50% SoC) with increasing numbers of mechanical fatigue cycles. After 1,000 cycles, the DC impedance of the *CFRP/No Rivet* cells was 123% of the initial value, while the corresponding values of the *MESC 4×4* and *MESC 5×5* cells were 102% and 103%, respectively. This finding also concurred with the capacity fading shown earlier; i.e., growth of higher DC impedance in the *CFRP/No Rivet* cell led to a degraded rate capability and thus to reduced capacity delivery. However, this impedance increase was not high enough to be the sole contributor to the capacity fading, particularly in the *CFRP/No Rivet* cells. Therefore, it was hypothesized that capacity fading was also partly due to loss of the active materials, e.g., flaking of electrode coatings and electrode layer misalignment caused by the cyclic deformation. Further investigations are being performed in conjunction with in-situ material characterizations to determine the underlying mechanisms for capacity fading due to mechanical fatigue. This work in progress also aims to evaluate how the capacity fading changes under different loading levels, amplitude ratios, and loading directions, and under combinations of electrical and mechanical cycling. The results will be helpful in understanding the mechano-electrical capabilities of MESCs and in construction of an operational envelope for this newly developed material system.

5. Conclusions

In this paper, we introduced multifunctional energy storage composites (MESCs), a novel form of structurally-integrated batteries fabricated in a unique material vertical integration process. The MESC architecture makes industry-standard Li-ion battery electrodes multifunctional by using their intrinsic mechanical properties, all without modification to the battery chemistry. The MESC construction uses through-thickness interlocking rivets to stabilize the loose electrode layers and anchor them securely to the encapsulating high-strength CFRP facesheets. The typical interlayer shear movement of the electrode

layers is prevented, thus allowing the layers to contribute to carrying of the mechanical load. This work has presented mechano-electrical characterization results for the first-generation MESC, which followed careful design and fabrication.

The MESC cells went through thorough preliminary characterization, including electrochemical reference testing, quasi-static three-point bending tests, and mechanical fatigue testing. When compared with state-of-the-art pouch Li-ion batteries, the MESCs with the rivet topologies used in this study demonstrated more than fifteen-fold improvement in their mechanical performance (in mechanical flexural rigidity and capacity-fading resistance under repeated mechanical loading) (Figure 7). The interlocking rivets prevented excessive deformation of the electrodes and thus inhibited any discernable electrochemical capacity degradation, even after 1,000 cycles under 700 N (200 lb) bending loads. This was achieved while sacrificing less than 40% of energy density compared to unprotected pouch cells and maintaining comparable electrochemical capabilities to the baseline chemistry in terms of charge/discharge characteristics and life cycle performance. Improvement in the fabrication process and cell architecture is underway to match the baseline performance on apparent capacity delivery, DC impedance, as well as cell-to-cell reproducibility and reliability.

Ultimately, it has been demonstrated that MESCs can simultaneously function as both energy storage units and load-carrying members through careful harnessing of these materials' inherent multifunctional capabilities. This new multifunctional structural battery can be a scalable building block for construction of structural components with built-in energy-storage capabilities. We already have taken the first step of constructing multi-cell MESC demonstrator modules, as shown in Figure 8 and Supplementary Movie S2 (Supplementary Information). Traditional unifunctional components can be replaced with similarly-sized energy-storage structures, resulting in significant weight and volume savings, enhanced packing factors, and reduced complexity. This material also has a spill-over effect in that it enables design flexibility and

new design paradigms that are not focused on centralized battery packs with boxy protective enclosures. This creates a disruptive but accelerated path to maximize battery performance and efficiency at the system level for EVs and other tangential applications.

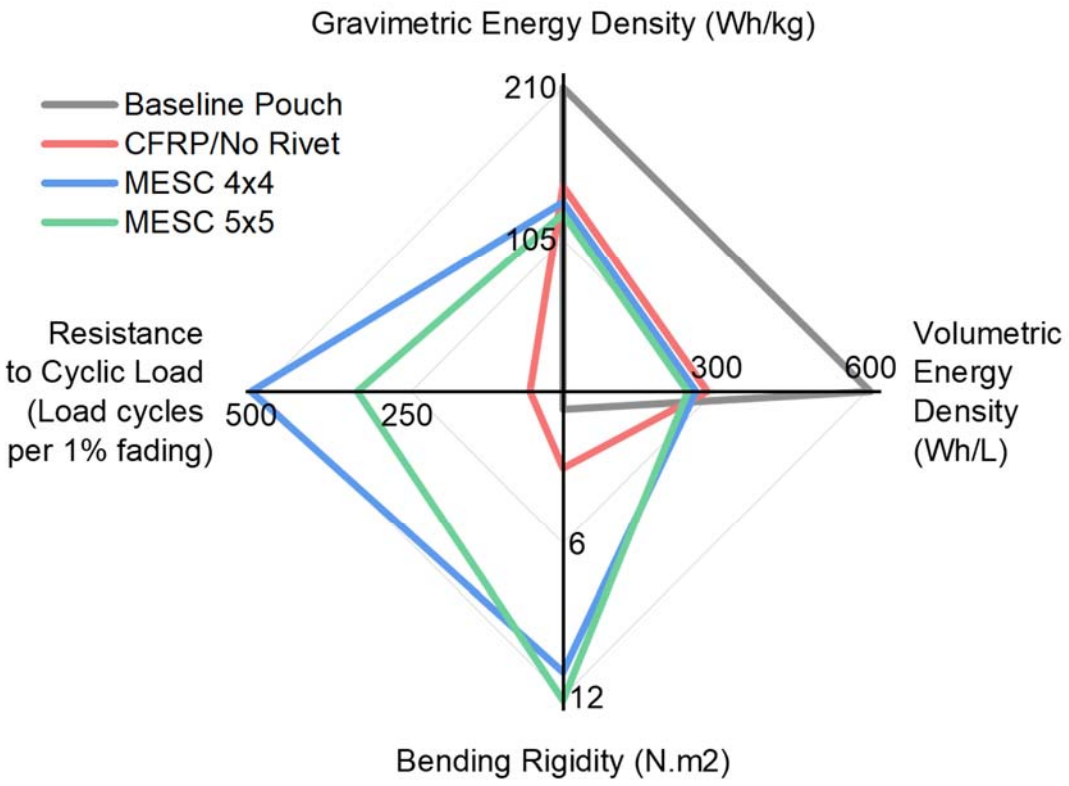

Figure 7. Comparison of figures of merit. At 130 Wh/kg and 260 Wh/L, the first-generation MESC shows significant improvements in mechanical performance over traditional pouch cells in terms of mechanical bending rigidity and electrochemical resistance to cyclic mechanical loading. The beneficial contributions of the interlocking rivets are strongly emphasized by comparing the results for the MESC with those of the nonriveted CFRP-reinforced counterpart (*CFRP/No Rivet*).

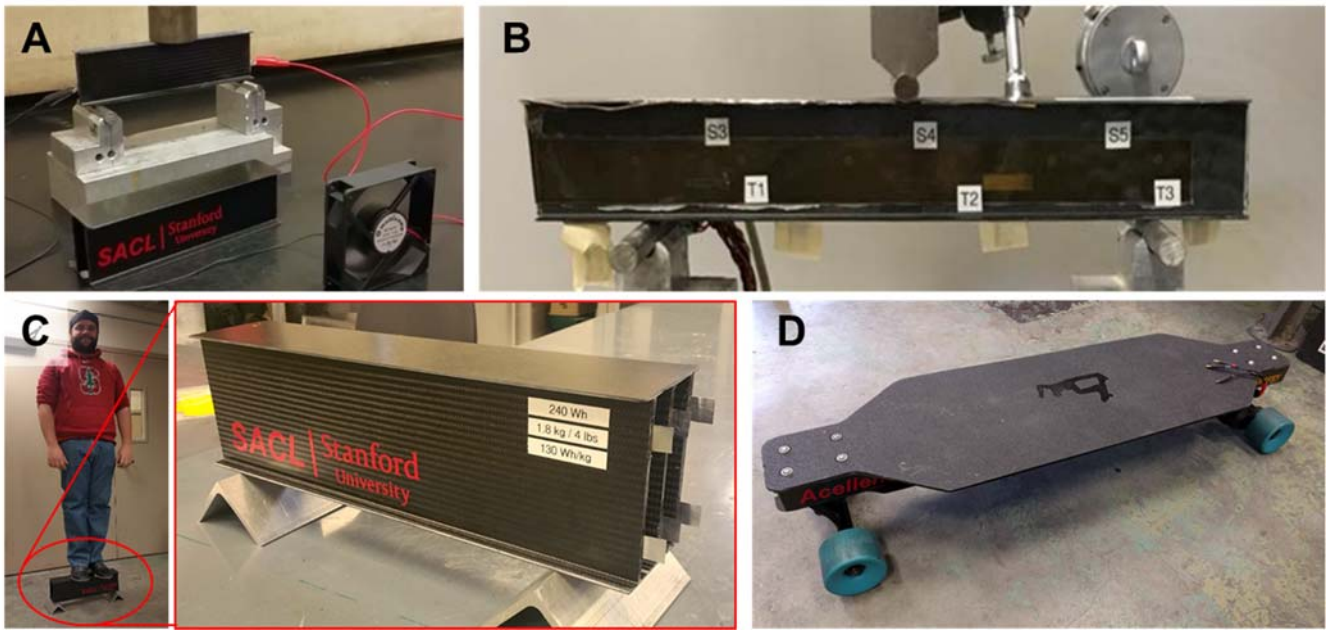

Figure 8. Scaled-up MESC prototypes demonstrating the material's versatility and scalability. A) Three-cell, 5 Wh MESC module in the form of a structural I-beam (30 cm long, 2.5 cm high); **B)** three-cell, 40 Wh MESC I-beam module (38 cm long, 4 cm high); **C)** 12-cell, 240 Wh MESC triple-webbed I-beam module (50 cm long, 13 cm high); **D)** 10-cell, 200 Wh electric skateboard with MESC-integrated deck.

6. Acknowledgements

This work was supported by the Advanced Research Projects Agency – Energy (U.S. Department of Energy) [grant number DE-AR0000393]. The authors greatly appreciate the support received from Dr. Keith Kepler, Dr. Hongjian Liu, and Dr. Michael Slater at Farasis Energy, Inc., who provided access to electrochemical testing facilities, and valuable feedback and suggestions throughout the fabrication process. The authors would also like to thank the Structures and Composites Laboratory's graduate students, Raunaq Rewari, Anthony Bombik, Yinan Wang, Alexander Strange, and Fabian Rothmaier, for

insightful discussions and their significant contributions to sample preparation and mechano-electrical testing.

7. References

1. Dunn, J., L. Gaines, J. Kelly, C. James, and K. Gallagher, *The significance of Li-ion batteries in electric vehicle life-cycle energy and emissions and recycling's role in its reduction.* Energy & Environmental Science, 2015. **8**(1): p. 158-168.
2. Tran, M., D. Banister, J.D. Bishop, and M.D. McCulloch, *Realizing the electric-vehicle revolution.* Nature climate change, 2012. **2**(5): p. 328.
3. Egbue, O. and S. Long, *Barriers to widespread adoption of electric vehicles: An analysis of consumer attitudes and perceptions.* Energy policy, 2012. **48**: p. 717-729.
4. Rauh, N., T. Franke, and J.F. Krems, *Understanding the impact of electric vehicle driving experience on range anxiety.* Human factors, 2015. **57**(1): p. 177-187.
5. Howell, D., *Battery status and cost reduction prospects.* US Dept Energy, 2012.
6. Eberle, U. and R. Von Helmolt, *Sustainable transportation based on electric vehicle concepts: a brief overview.* Energy & Environmental Science, 2010. **3**(6): p. 689-699.
7. Wagner, F.T., B. Lakshmanan, and M.F. Mathias, *Electrochemistry and the future of the automobile.* J. Phys. Chem. Lett, 2010. **1**(14): p. 2204-2219.
8. Neubauer, J., A. Pesaran, C. Bae, R. Elder, and B. Cunningham, *Updating United States Advanced Battery Consortium and Department of Energy battery technology targets for battery electric vehicles.* Journal of Power Sources, 2014. **271**: p. 614-621.

9. Thackeray, M.M., C. Wolverton, and E.D. Isaacs, *Electrical energy storage for transportation—approaching the limits of, and going beyond, lithium-ion batteries.* Energy & Environmental Science, 2012. **5**(7): p. 7854-7863.
10. Scrosati, B., J. Hassoun, and Y.-K. Sun, *Lithium-ion batteries. A look into the future.* Energy & Environmental Science, 2011. **4**(9): p. 3287-3295.
11. Szczech, J.R. and S. Jin, *Nanostructured silicon for high capacity lithium battery anodes.* Energy & Environmental Science, 2011. **4**(1): p. 56-72.
12. Scrosati, B. and J. Garche, *Lithium batteries: Status, prospects and future.* Journal of Power Sources, 2010. **195**(9): p. 2419-2430.
13. Howell, D., B. Cunningham, T. Duong, and P. Faguy, *Overview of the DOE VTO advanced battery R&D program.* Annual Merit Review June, 2016. **6**.
14. Mikolajczak, C., M. Kahn, K. White, and R.T. Long, *Lithium-ion batteries hazard and use assessment*. 2012: Springer Science & Business Media.
15. Xia, Y., T. Wierzbicki, E. Sahraei, and X. Zhang, *Damage of cells and battery packs due to ground impact.* Journal of Power Sources, 2014. **267**: p. 78-97.
16. Andrea, D., *Battery management systems for large lithium ion battery packs*. 2010: Artech house.
17. Albertus, P., *RANGE concepts beyond the RANGE program*, in *ARPA-E Robust Affordable Next Generation Energy Storage Systems (RANGE) Annual Program Review* 2016: Fort Lauderdale, FL.
18. Sahraei, E., R. Hill, and T. Wierzbicki, *Calibration and finite element simulation of pouch lithium-ion batteries for mechanical integrity.* Journal of Power Sources, 2012. **201**: p. 307-321.
19. Thomas, J.P. and M.A. Qidwai, *Mechanical design and performance of composite multifunctional materials.* Acta Materialia, 2004. **52**(8): p. 2155-2164.

20. Thomas, J.P. and M.A. Qidwai, *The design and application of multifunctional structure-battery materials systems.* Jom, 2005. **57**(3): p. 18-24.

21. Christodoulou, L. and J.D. Venables, *Multifunctional material systems: The first generation.* JOM, 2003. **55**(12): p. 39-45.

22. Lyman, P.C. and T.L. Feaver, *PowerCore combining structure and batteries for increased energy to weight ratio.* IEEE aerospace and electronic systems magazine, 1998. **13**(9): p. 39-42.

23. Liu, P., E. Sherman, and A. Jacobsen, *Design and fabrication of multifunctional structural batteries.* Journal of Power Sources, 2009. **189**(1): p. 646-650.

24. Snyder, J.F., E.L. Wong, and C.W. Hubbard, *Evaluation of commercially available carbon fibers, fabrics, and papers for potential use in multifunctional energy storage applications.* Journal of the Electrochemical Society, 2009. **156**(3): p. A215-A224.

25. Roberts, S.C. and G.S. Aglietti, *Structural performance of a multifunctional spacecraft structure based on plastic lithium-ion batteries.* Acta Astronautica, 2010. **67**(3-4): p. 424-439.

26. Pereira, T., Z. Guo, S. Nieh, J. Arias, and H.T. Hahn, *Embedding thin-film lithium energy cells in structural composites.* Composites Science and Technology, 2008. **68**(7-8): p. 1935-1941.

27. Kjell, M.H., E. Jacques, D. Zenkert, M. Behm, and G. Lindbergh, *PAN-based carbon fiber negative electrodes for structural lithium-ion batteries.* Journal of The Electrochemical Society, 2011. **158**(12): p. A1455-A1460.

28. Qian, H., A.R. Kucernak, E.S. Greenhalgh, A. Bismarck, and M.S. Shaffer, *Multifunctional structural supercapacitor composites based on carbon aerogel modified high performance carbon fiber fabric.* ACS applied materials & interfaces, 2013. **5**(13): p. 6113-6122.

29. Asp, L.E. and E.S. Greenhalgh, *Structural power composites.* Composites science and technology, 2014. **101**: p. 41-61.

30. Zhang, Y., J. Ma, A.K. Singh, L. Cao, J. Seo, C.D. Rahn, C.E. Bakis, and M.A. Hickner, *Multifunctional structural lithium-ion battery for electric vehicles.* Journal of Intelligent Material Systems and Structures, 2017. **28**(12): p. 1603-1613.
31. Gasco, F. and P. Feraboli, *Manufacturability of composite laminates with integrated thin film Li-ion batteries.* Journal of Composite Materials, 2014. **48**(8): p. 899-910.
32. Mullenax, J., P. Browning, W. Huebsch, M. Gautam, and E.M. Sabolsky, *Composite Multifunctional Lithium-Ion Batteries.* ECS Transactions, 2012. **41**(41): p. 175-185.
33. Anton, S., A. Erturk, and D. Inman, *Multifunctional self-charging structures using piezoceramics and thin-film batteries.* Smart materials and Structures, 2010. **19**(11): p. 115021.
34. Kim, H.C. and A.M. Sastry, *Effects of carbon fiber electrode deformation in multifunctional structural lithium ion batteries.* Journal of Intelligent Material Systems and Structures, 2012. **23**(16): p. 1787-1797.
35. Tsutsui, W., T. Nguyen, H. Liao, N. Parab, J. Kukreja, T. Siegmund, and W. Chen, *Mechanical energy dissipation in a multifunctional battery system.* MRS Advances, 2016. **1**(6): p. 381-388.
36. Neudecker, B.J., M.H. Benson, and B.K. Emerson, *Power fibers: Thin-film batteries on fiber substrates*. 2003, ITN ENERGY SYSTEMS INC LITTLETON CO.
37. Snyder, J., E. Gienger, and E. Wetzel, *Performance metrics for structural composites with electrochemical multifunctionality.* Journal of Composite Materials, 2015. **49**(15): p. 1835-1848.
38. Shirshova, N., H. Qian, M.S. Shaffer, J.H. Steinke, E.S. Greenhalgh, P.T. Curtis, A. Kucernak, and A. Bismarck, *Structural composite supercapacitors.* Composites Part A: Applied Science and Manufacturing, 2013. **46**: p. 96-107.

39. Senokos, E., Y. Ou, J.J. Torres, F. Sket, C. González, R. Marcilla, and J.J. Vilatela, *Energy storage in structural composites by introducing CNT fiber/polymer electrolyte interleaves.* Scientific reports, 2018. **8**(1): p. 3407.

40. Adam, T.J., G. Liao, J. Petersen, S. Geier, B. Finke, P. Wierach, A. Kwade, and M. Wiedemann, *Multifunctional Composites for Future Energy Storage in Aerospace Structures.* Energies, 2018. **11**(2): p. 335.

41. Singh, A.K., L. Cao, J. Ma, J. Seo, C.E. Bakis, Y. Zhang, M.A. Hickner, and C.D. Rahn, *Design, manufacture and test of a novel structural battery based on sandwich construction.* Journal of Sandwich Structures & Materials, 2015. **17**(6): p. 666-690.

42. Thomas, J.P. and M.A. Qidwai, *The design and application of multifunctional structure-battery materials systems.* JOM Journal of the Minerals, Metals and Materials Society, 2005. **57**(3): p. 18-24.

43. Thomas, J., S. Qidwai, W. Pogue III, and G. Pham, *Multifunctional structure-battery composites for marine systems.* Journal of Composite Materials, 2013. **47**(1): p. 5-26.

44. Kukreja, J., T. Nguyen, T. Siegmund, W. Chen, W. Tsutsui, K. Balakrishnan, H. Liao, and N. Parab, *Crash analysis of a conceptual electric vehicle with a damage tolerant battery pack.* Extreme Mechanics Letters, 2016. **9**: p. 371-378.

45. Snyder, J.F., R.H. Carter, and E.D. Wetzel, *Electrochemical and mechanical behavior in mechanically robust solid polymer electrolytes for use in multifunctional structural batteries.* Chemistry of materials, 2007. **19**(15): p. 3793-3801.

46. Willgert, M., M.H. Kjell, G. Lindbergh, and M. Johansson, *New structural lithium battery electrolytes using thiol–ene chemistry.* Solid State Ionics, 2013. **236**: p. 22-29.

47. Shirshova, N., A. Bismarck, S. Carreyette, Q.P. Fontana, E.S. Greenhalgh, P. Jacobsson, P. Johansson, M.J. Marczewski, G. Kalinka, and A.R. Kucernak, *Structural supercapacitor electrolytes based on bicontinuous ionic liquid–epoxy resin systems.* Journal of Materials Chemistry A, 2013. **1**(48): p. 15300-15309.

48. Stephan, A.M., K.S. Nahm, T.P. Kumar, M.A. Kulandainathan, G. Ravi, and J. Wilson, *Nanofiller incorporated poly (vinylidene fluoride–hexafluoropropylene)(PVdF–HFP) composite electrolytes for lithium batteries.* Journal of power sources, 2006. **159**(2): p. 1316-1321.

49. Agrawal, R., A. Chandra, A. Bhatt, and Y. Mahipal, *Investigations on ion transport properties of and battery discharge characteristic studies on hot-pressed Ag+-ion-conducting nano-composite polymer electrolytes:(1–x)[90PEO: 10AgNO3]: xSiO2.* New Journal of Physics, 2008. **10**(4): p. 043023.

50. Carlson, T., D. Ordéus, M. Wysocki, and L.E. Asp, *Structural capacitor materials made from carbon fibre epoxy composites.* Composites Science and Technology, 2010. **70**(7): p. 1135-1140.

51. Jacques, E., M.H. Kjell, D. Zenkert, G. Lindbergh, M. Behm, and M. Willgert, *Impact of electrochemical cycling on the tensile properties of carbon fibres for structural lithium-ion composite batteries.* Composites Science and Technology, 2012. **72**(7): p. 792-798.

52. Lin, Y. and H.A. Sodano, *Characterization of multifunctional structural capacitors for embedded energy storage.* Journal of Applied Physics, 2009. **106**(11): p. 114108.

53. Sahraei, E., J. Meier, and T. Wierzbicki, *Characterizing and modeling mechanical properties and onset of short circuit for three types of lithium-ion pouch cells.* Journal of Power Sources, 2014. **247**: p. 503-516.

54. Allen, H.G., *Analysis and design of structural sandwich panels: the commonwealth and international library: structures and solid body mechanics division*. 2013: Elsevier.

55. Vinson, J.R., *The behavior of sandwich structures of isotropic and composite materials*. 1999: CRC Press.

56. Johnson, R. and I. May, *Partial-interaction design of composite beams.* Structural Engineer, 1975. **8**(53).

57. Viest, I. *Investigation of stud shear connectors for composite concrete and steel T-beams*. in *Journal Proceedings*. 1956.

58. Wang, Y., *Deflection of steel-concrete composite beams with partial shear interaction.* Journal of Structural Engineering, 1998. **124**(10): p. 1159-1165.

59. Christophersen, J., *Battery Test Manual For Electric Vehicles.* Idaho National Laboratory, 2015.

60. *C393–00. Standard Test Method for Flexural Properties of Sandwich Constructions.* ASTM C393, 2000.

61. *D7250.* Standard Practice for Determining Sandwich Beam Flexural and Shear Stiffness. ASTM International, 2006. **18**: p. 68.

62. Lewerenz, M., J. Münnix, J. Schmalstieg, S. Käbitz, M. Knips, and D.U. Sauer, *Systematic aging of commercial LiFePO4| Graphite cylindrical cells including a theory explaining rise of capacity during aging.* Journal of Power Sources, 2017. **345**: p. 254-263.

63. Gyenes, B., D. Stevens, V. Chevrier, and J. Dahn, *Understanding anomalous behavior in coulombic efficiency measurements on Li-ion batteries.* Journal of The Electrochemical Society, 2015. **162**(3): p. A278-A283.

Supplementary Information

Multifunctional Energy Storage Composite Structures with Embedded Lithium-ion Batteries

Purim Ladpli[a†], Raphael Nardari[a], Fotis Kopsaftopoulos[b], Fu-Kuo Chang[a]

[a] Department of Aeronautics and Astronautics, Stanford University, Stanford, CA 94305, USA

[b] Department of Mechanical, Aerospace and Nuclear Engineering, Rensselaer Polytechnic Institute, Troy, NY 12180, USA

[†] Corresponding author. Email: pladpli@stanford.edu; Address: Durand Building, Room 054, 496 Lomita Mall, Stanford University, Stanford, CA 94305, USA; Tel: +1 (650) 723-3524

Supplementary Data:

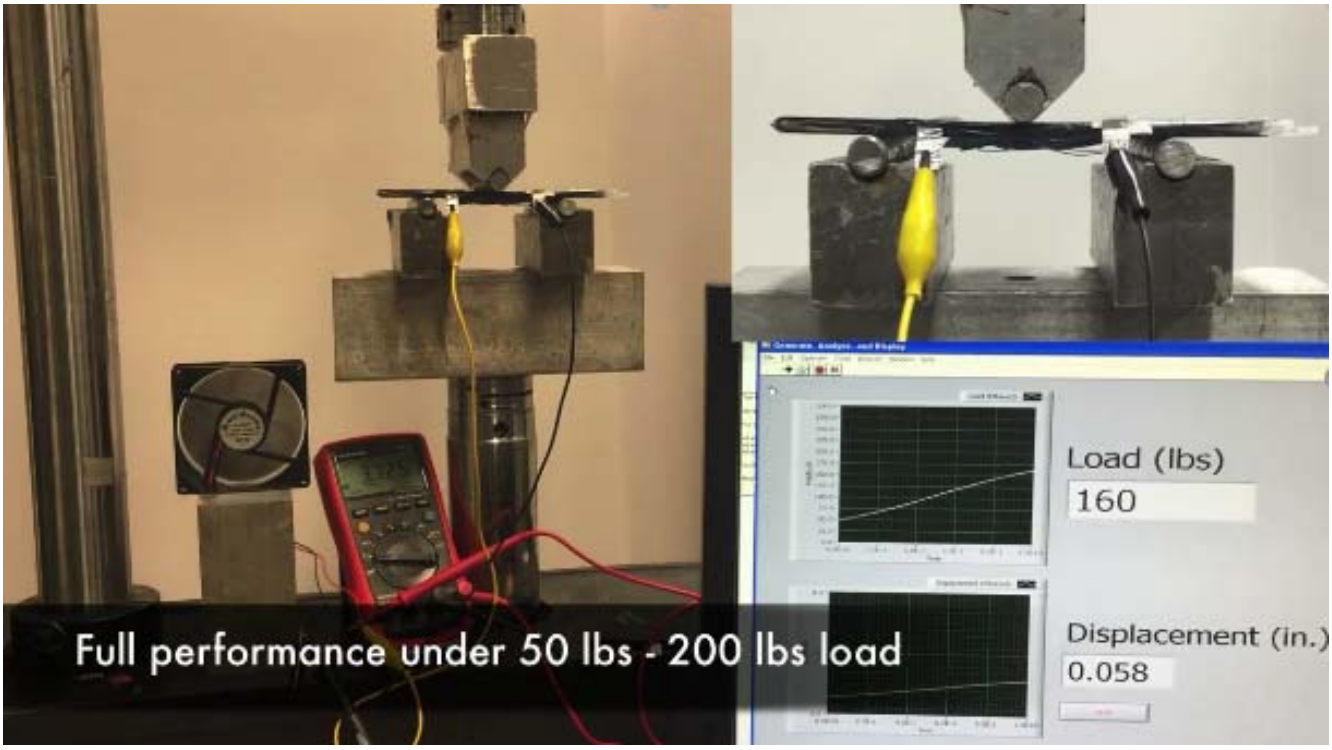

Supplementary Movie S1. Movie showing an *MESC 4×4* cell under cyclic three-point bending with a maximum load of 700 N, where the cell's electrical functionality is also shown by powering a DC fan and maintaining the appropriate cell voltage throughout the experiment.

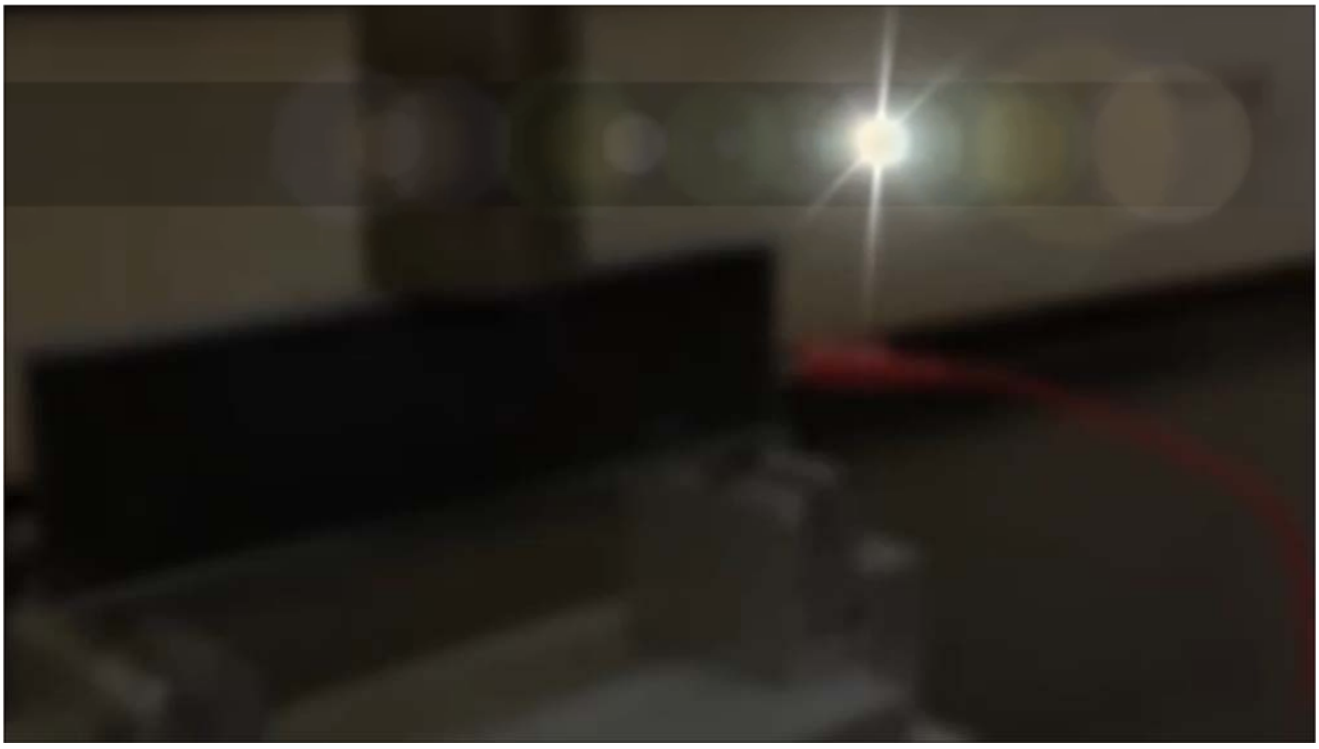

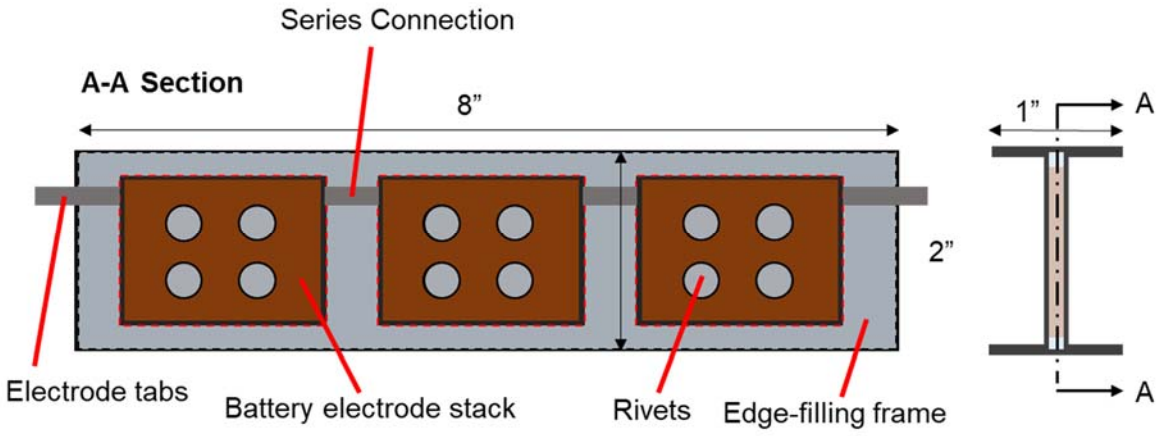

Supplementary Movie S2. Movie showing MESC multi-cell module in a structural I-beam construction (8” × 2” × 1”) simultaneously storing/supplying electrical energy to a 12VDC fan and carrying a mechanical bending load. The I-beam is a three-cell (3S (three cells in series)) MESC module with a nominal voltage of 11.1V, and 5.1Wh theoretical energy. Each cell in the string is a 21-layer cell measured 1.71” × 1.22” with four 0.4”-diameter perforations with a nominal capacity of 0.46 Ah.

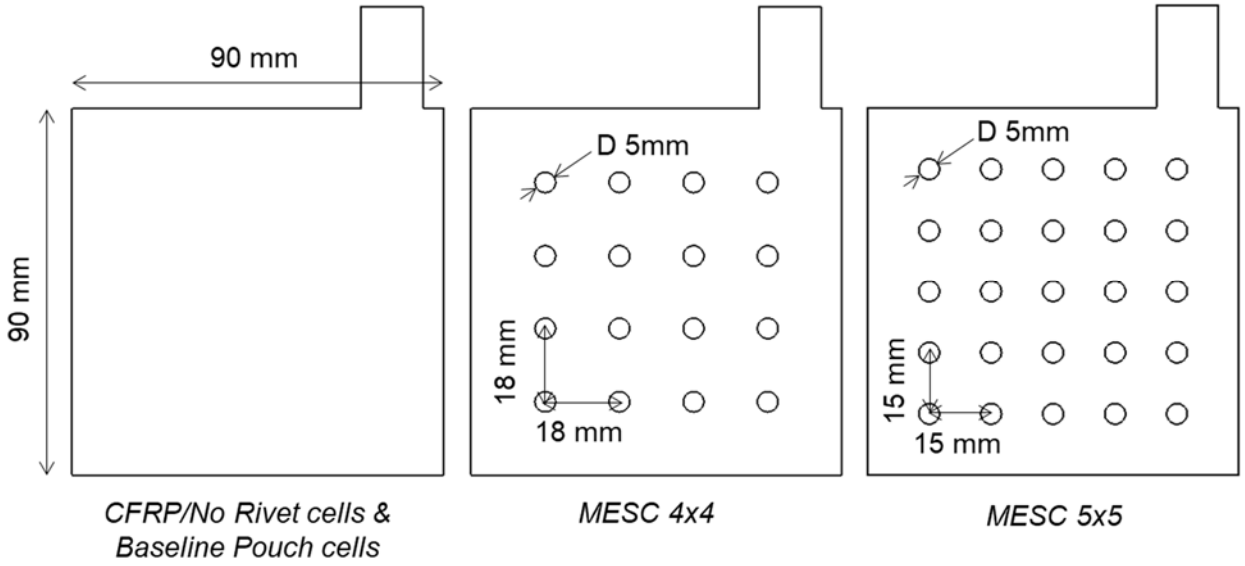

Figure S 1. Electrode punch geometry as measured on the anode. All sample types share the same outer electrode footprint of 90 mm × 90 mm as measured on the anode. The anode in the *MESC 4×4* and *MESC 5×5* has a 4×4 array and a 5×5 array of 5 mm-diameter holes, respectively. The cathode is measured 0.5mm in every dimension; i.e. the outer square dimension measures 89 mm × 89 mm, while the holes are 6 mm in diameter.

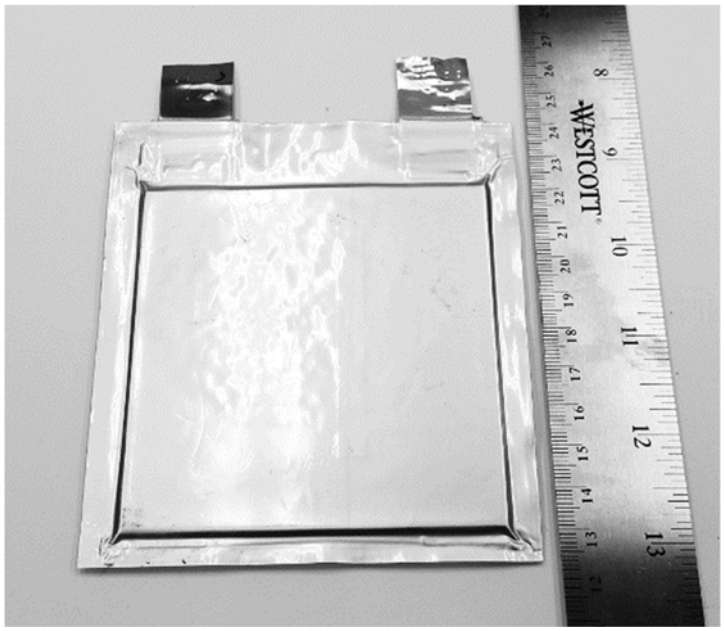

Figure S 2. Image of a representative *Baseline Pouch* cell. The *Baseline Pouch* cells use the same nonperforated electrode stack as the *CFRP/No Rivet* cells, but they are packaged in conventional aluminum-polymer-laminate packaging.

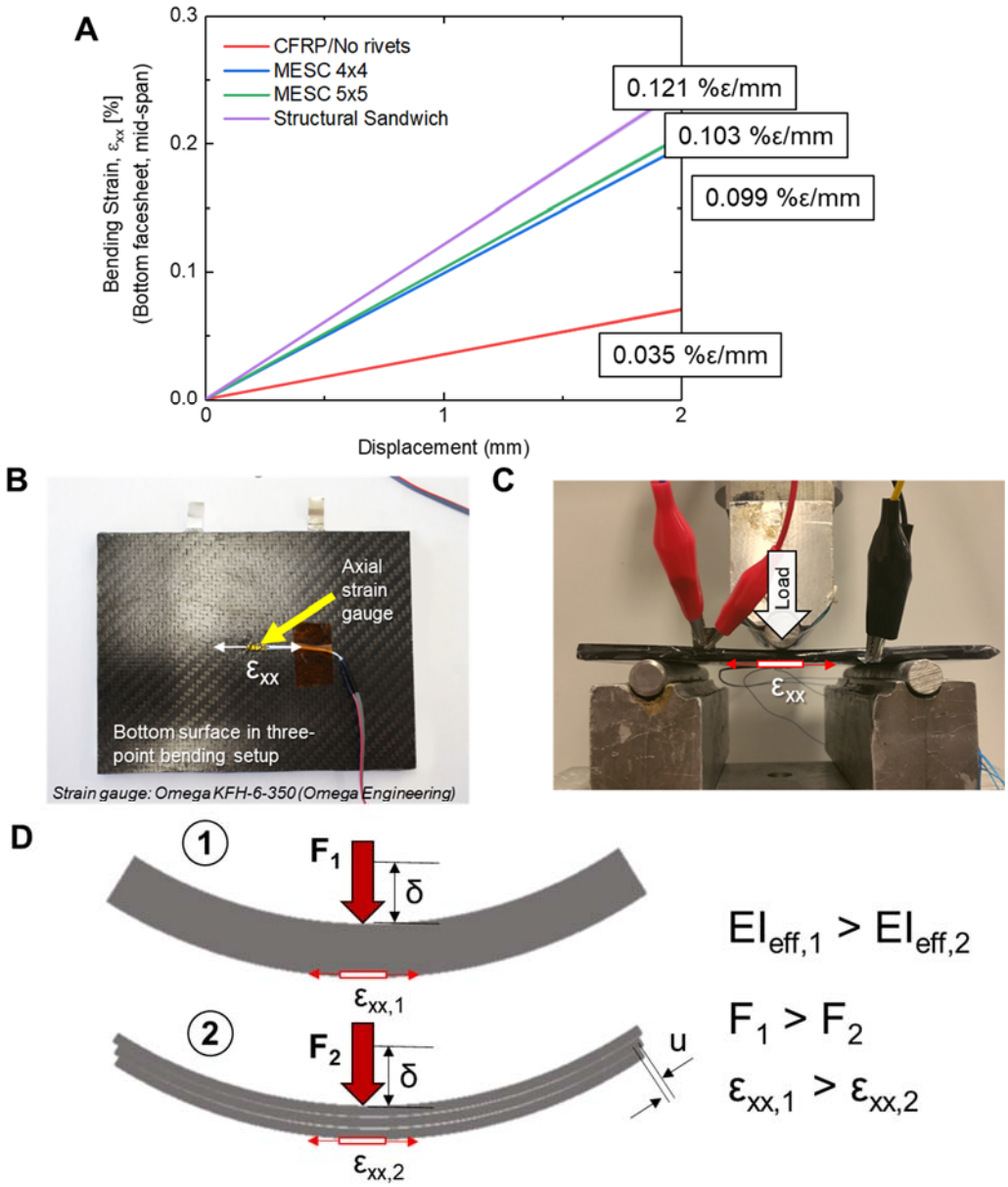

Figure S 3. Bending normal strain on CFRP during quasi-static 3pt-bending experiment. A) maximum bending normal strain -vs- mid-span displacement for different sample types obtained using surface-mounted strain gauges. The larger the bending strain is observed at a given mid-span deflection, the higher CFRP utilization efficiency, which is an indication of better shear transfer through the sandwich core, **B)** location of the strain gauge on the cells, **C)** schematic showing the bending normal strain measurement during the 3pt-bending load application. The strain gauges were mounted at the center of the outer surface of the bottom CFRP facesheet with the axial direction of the strain gauge aligned with the

longitudinal direction of the 3pt-bending setup. Located the furthest away from the neutral axis, the maximum bending normal strain in the laminate was measured and compared, **D)** a simple schematic showing how bending strain relates to the degree of interaction between the layers of a laminate under bending, and hence to the bending rigidity of the laminate.

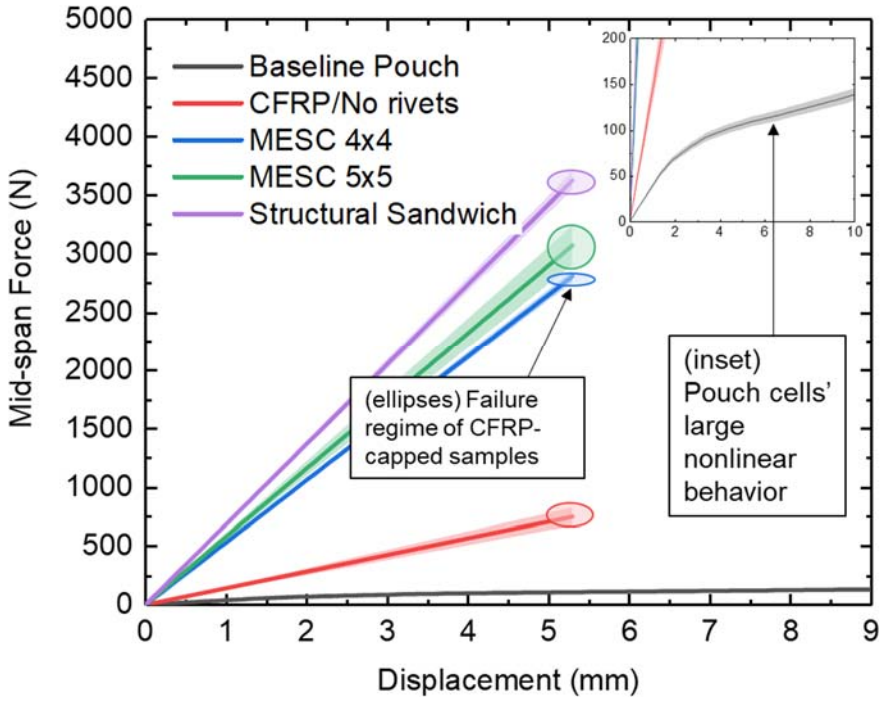

Figure S 4. Complete up-to-failure load-displacement curves. The complete load-displacement curves observed during the quasi-static 3pt-bending experiment are shown for all the different types of samples, **CFRP-encapsulated Samples.** The CFRP-encapsulated samples showed a linear load-displacement relationship up to the point of failure. The failure of the CFRP-encapsulated samples was consistently found to take place when the mid-span displacement reached 5 - 5.5 mm, which was accompanied by the disbond of the bottom facesheet from the edge-filling frame, **Pouch Cells.** A highly non-linear load-displacement relationship was instead observed for the *Baseline Pouch* cell counterpart starting from mid-span displacement > 2mm, as shown in greater detail in the inset. The shaded areas around the lines represent the standard deviation of five replicate samples.

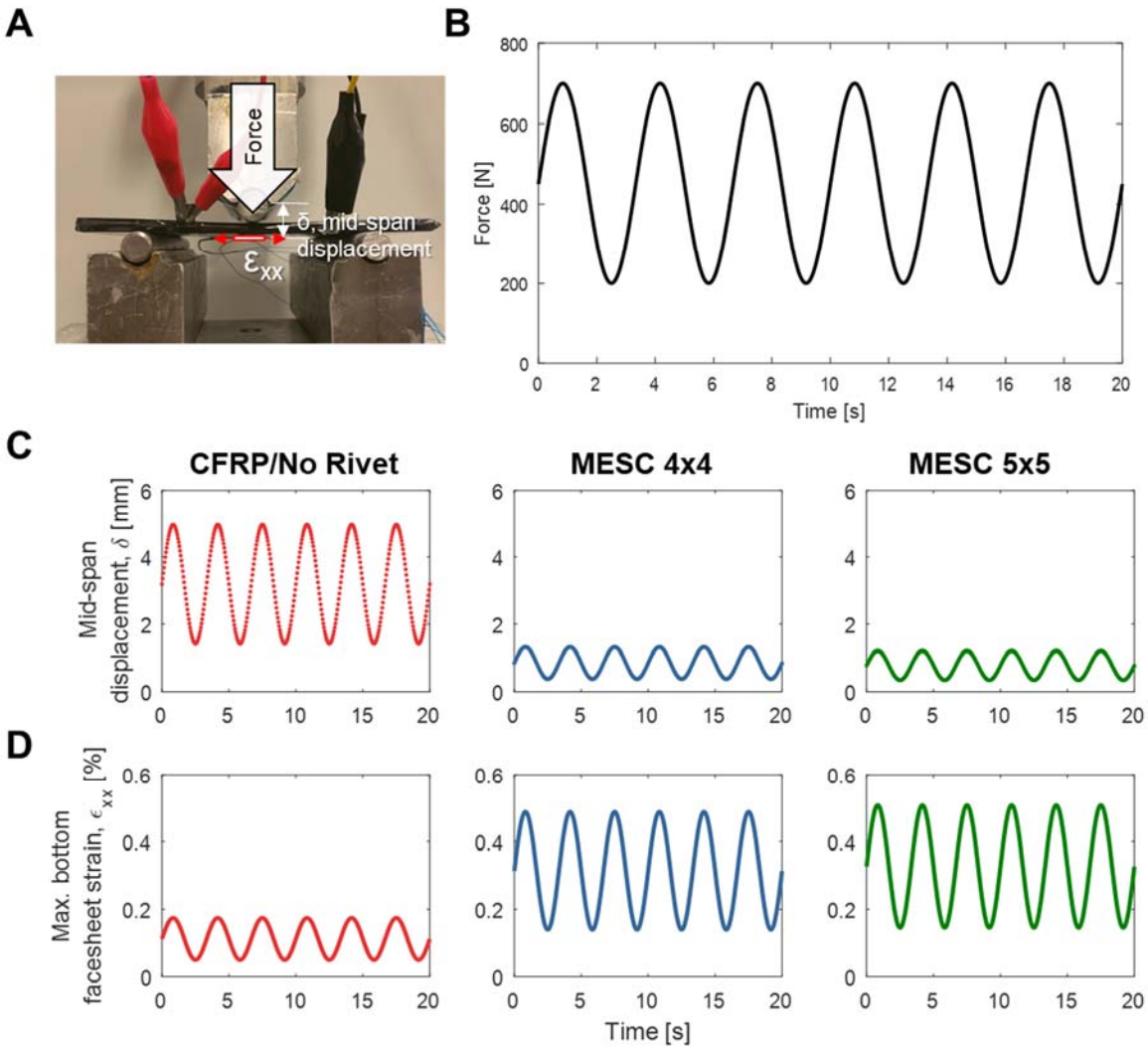

Figure S 5. Cyclic response of the load, mid-span deflection, and bending strain measurements during the mechanical fatigue test. A) location of the strain measurement showing the maximum bending strain being measured, **B)** the time history of the cyclic load application, **C)** the resulting mid-span deflection of the three different sample types with the CFRP/No Rivet samples having the least resistance to bending, **D)** the resulting bending strain on the outer surface of the bottom facesheet.

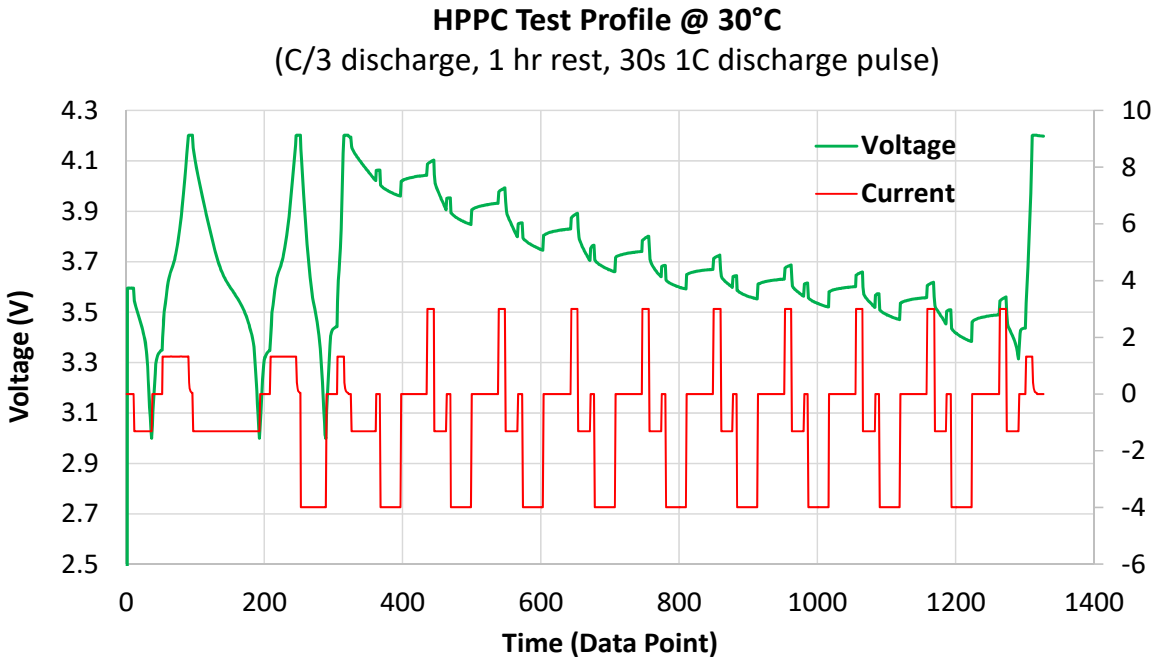

Figure S 6. HPPC Test Profile. The HPPC test profile was derived from the USABC's Battery Test Manual for Electric Vehicles. The test profile includes a full discharge at C/3 rate followed by a series of discharge and regen (charge) pulses at every 10 % increment of the battery state of charge. The HPPC test is intended to determine the dynamic power capability of the battery with references to actual EV applications. The periodic interruptions of the charge/discharge current allow the DC impedance of the battery to be evaluated.

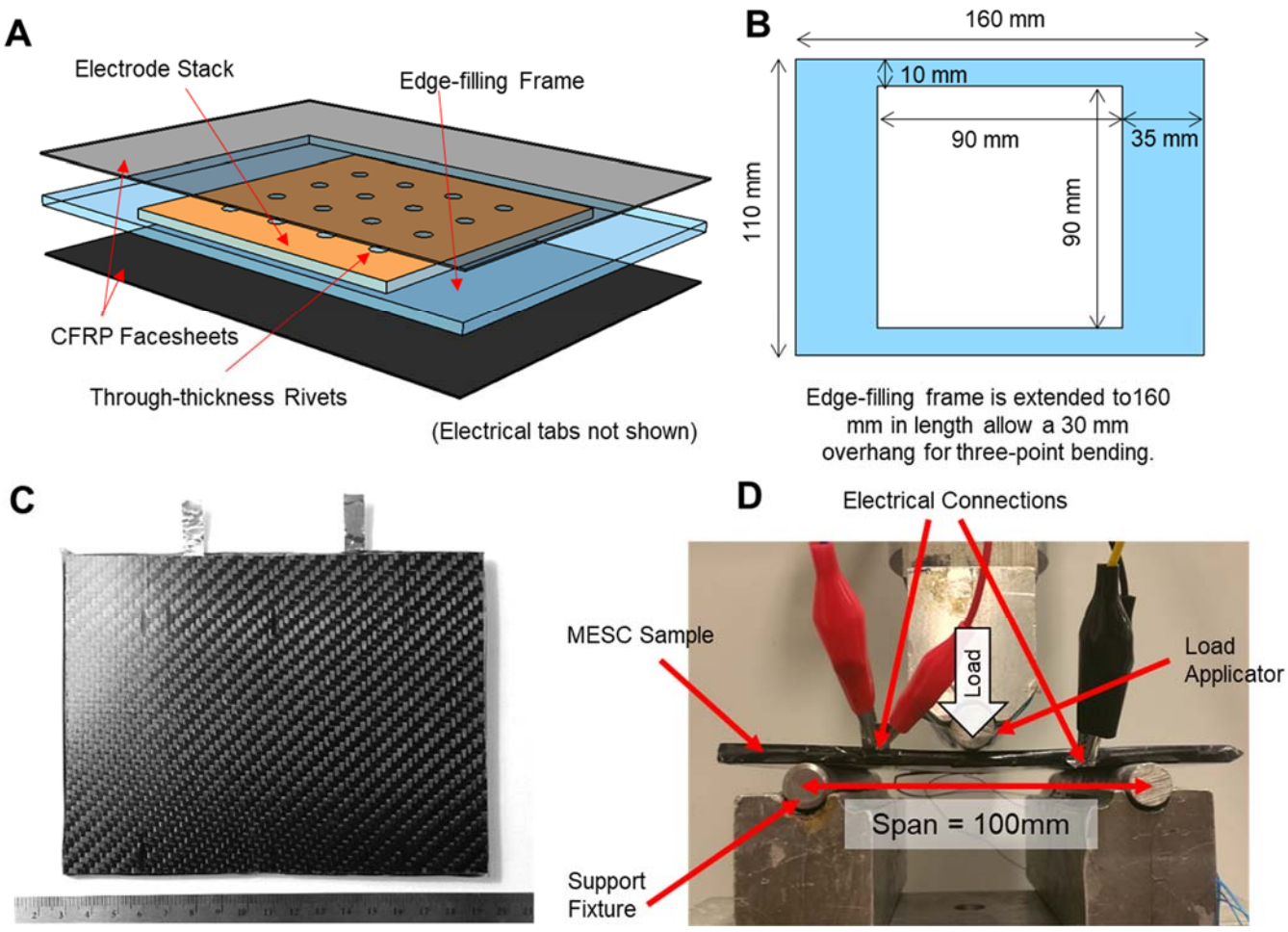

Figure S 7. Details and dimensions of the mechanical 3pt-bending CFRP-encapsulated samples. A) a 3D schematic of an *MESC 4×4* cell showing the same square battery stack sitting in the middle of an enlarged edge-filling frame. The edge-filling frame is elongated in the longitudinal direction of the three-point bending setup to allow for an overhang, B) dimensions of the enlarged edge-filling frame, C) image of an as-fabricated 3pt-bending CFRP-encapsulated samples, D) three-point bending setup with the supporting span dimension labelled showing the sample extending/overhanging beyond the supports.

Remarks on the Three-Point Bending Test

The two supports were equally spaced and separated by a 100-mm span. Note that the *MESC* and *CFRP/No Rivet* samples for the three-point-bending test were extended in length to 160 mm to allow for overhangs. The overhung portion were made with enlarged edge filling frames and CFRP, and therefore did not affect the electrochemical performance. The span allowed for an overhang of 30 mm on either side of the samples (lengthwise direction). The support span was approximately 20 times the thickness of the samples, which was sufficient to avoid considerable influence from transverse shear.

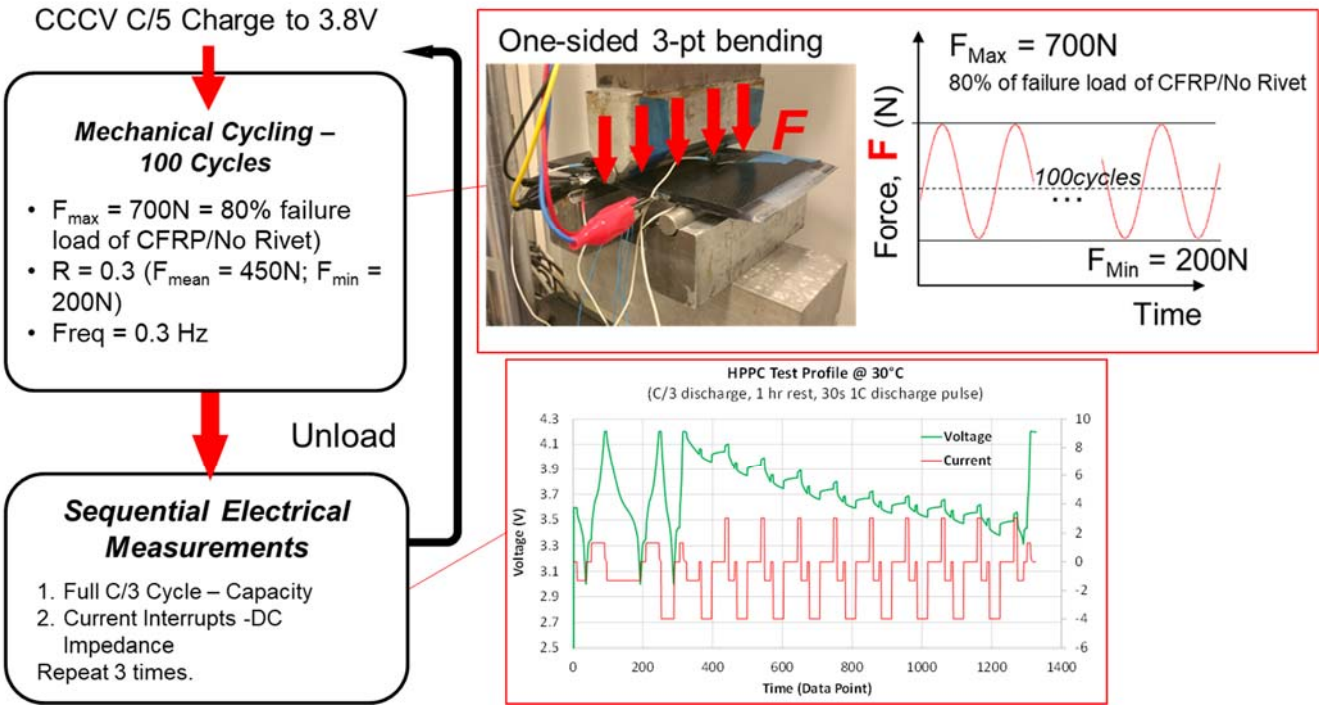

Figure S 8. Mechanical fatigue test flow chart. Each sample undergoes 100 cycles of single-sided bending load application (F_{max} = 700 N, R = 0.3, and f = 0.3 Hz). After each 100 cycles, the mechanical testing is stopped, and the cell is brought back to perform the sequential electrical measurements, which includes a full C/3 cycle and an HPPC test profile. The cell is then conditioned to 3.8V OCV before another 100 cycles of mechanical fatigue is performed and so on for a total of 1,000 mechanical cycles.

Table S 1. Electrochemical data as shown in Figure 4.

A

Sample	Theoretical Capacity [mAh]	Measured Capacity [mAh]	
		Capacity	Std. Dev.
Baseline Pouch	4602	4602	92
CFRP/No rivets	4602	4510	90
MESC 4x4	4340	4243	85
MESC 5x5	4192	3974	79

B

Sample	Measured Energy [Wh] (3.7 V Nominal)	Gravimetric Energy Density		Volumetric Energy Density	
		Weight [g]	Energy Density [Wh/kg]	Volume [mm3]	Energy Density [Wh/L]
Baseline Pouch	17.0	81	210	28350	601
CFRP/No rivets	16.7	120	139	60500	276
MESC 4x4	15.7	120	131	60500	260
MESC 5x5	14.7	120	123	60500	243

C

Sample	DC Impedance [mΩ] @ X % DoD								
	10%	20%	30%	40%	50%	60%	70%	80%	90%
Baseline Pouch	23.6	24.3	24.8	25.0	23.7	21.4	21.5	22.2	24.0
CFRP/No rivets	33.7	34.3	34.3	34.3	32.0	30.9	31.6	33.6	42.5
MESC 4x4	34.7	35.2	35.3	34.6	31.0	31.3	32.5	35.6	46.9
MESC 5x5	35.0	35.6	35.7	34.9	31.5	31.6	33.1	36.8	52.0

*Note: error approximately 1 mΩ across different samples and DoD

D

Sample	Capacity Retention [%] @ X cycles								
	0	100	200	300	400	500	600	700	800
Baseline Pouch	100.00	98.02	95.69	93.28	90.79	88.22	85.56	82.82	80.00
CFRP/No rivets	100.00	99.31	97.75	95.79	93.43	90.66	87.50	83.93	79.96

*Note: error approximately 0.0025 % x nCycles for Baseline Pouch cells and 0.005 % x nCycles for MESC.
e.g. error of MESC's capacity retention at 800th cycle = 0.005 % x 800 = 4 %

Table S 2. Mechanical-electrical data from the quasi-static three-point bending test as shown in Figure 5.

A

Sample	Linear slope between 0 - 0.5 mm displacement [N/mm]		Bending Rigidity [N·m^2] ($EI_{eff} = L^3/48$ x slope; L = 100 mm)	
	Slope	Std. Dev.	EI_{eff}	Std. Dev.
Baseline Pouch	34.6	1.9	0.7	0.04
CFRP/No rivets	141.4	14.9	3.0	0.3
MESC 4x4	530.0	9.5	11.0	0.2
MESC 5x5	580.0	31.8	12.1	0.7
Structural Sandwich	684.4	15.0	14.3	0.3

B

Sample	Discharge capacity under quasi-static load [% capacity at 0 mm]	
	1 mm mid-span	2 mm mid-span
CFRP/No rivets	100.5% ± 0.2%	98.4% ± 0.5%
MESC 4x4	99.3% ± 0.5%	98.9% ± 0.3%
MESC 5x5	101.2% ± 0.7%	100.7% ± 0.3%

C

Sample	DC impedance quasi-static load [% impedance at 0 mm]	
	1 mm mid-span	2 mm mid-span
CFRP/No rivets	102.2% ± 3.4%	97.8% ± 3.4%
MESC 4x4	100.8% ± 2.3%	104.2% ± 4.8%
MESC 5x5	97.0% ± 2.2%	100.9% ± 5.2%

Table S 3. Electrical data from the mechanical three-point bending fatigue test as shown in Figure 6.

A

Sample	Capacity Retention [% 0^{th} cycle] @ X^{th} mechanical cycle										
	0th	100th	200th	300th	400th	500th	600th	700th	800th	900th	1000th
CFRP/No rivets	100.0%	95.0%	92.8%	90.7%	90.4%	86.9%	85.7%	84.2%	83.3%	82.8%	81.4%
MESC 4x4	100.0%	99.4%	98.9%	98.6%	98.8%	98.1%	98.4%	98.0%	98.2%	98.2%	98.0%
MESC 5x5	100.0%	98.3%	98.3%	98.7%	98.6%	97.4%	97.5%	97.4%	97.4%	97.4%	97.2%

*Note: error approximately 2 % across different samples and cycle count

B

Sample	DC Impedance [% 0^{th} cycle] @ X^{th} mechanical cycle										
	0th	100th	200th	300th	400th	500th	600th	700th	800th	900th	1000th
CFRP/No rivets	100.0%	101.8%	101.8%	107.5%	105.0%	109.5%	113.4%	115.8%	118.2%	119.4%	120.4%
MESC 4x4	100.0%	100.7%	101.0%	100.0%	100.7%	104.0%	104.7%	101.5%	100.0%	100.7%	100.7%
MESC 5x5	100.0%	102.7%	101.4%	100.0%	101.4%	104.5%	105.5%	102.7%	103.2%	101.4%	101.8%

*Note: error approximately 3 % across different samples and cycle count

Supplementary Fabrication Methods:

Core Battery Stack

1. The electrode layers were received in a roll format, coated with active materials on both sides of the current collector (graphite (96 μm thick) on copper foil (10 μm) and NMC (60 μm) on aluminum foil (10 μm), respectively) (Farasis Energy, Inc.). The separator used in this study was a tri-layer polyolefin separator (PP/PE) (25 μm) (Farasis Energy, Inc.).
2. The electrode sheets were cut with steel rule dies using a pneumatic die cutting machine (BioCut Systems). Steel rule dies were made with the pre-designed dimensions (Figure S1).
3. The electrode stacking was performed in a Z-fold pattern. The stacking was done on an in-house alignment jig to ensure the stacking precision. The separator dispensing was assisted by the use of a manual separator dispensing machine for layer-by-layer pouch cells (MTI Corporation)
4. A desktop 800W ultrasonic metal welding machine (MTI Corporation) was used to weld metallic tabs on to the current collector foils (nickel tabs on copper, and aluminum tabs on aluminum current collectors).
5. The materials were allowed to dry in a vacuum oven for >48 hours prior to each step (electrodes at 80°C. Stacks at 50°C).

Structural Facesheets / Edge Filling Frames

1. The CFRP sheets were cut into size then primed with an adhesion promoter MICA G-1092 according to the manufacturer's recommended procedure (MICA Corp.).

2. The EAA pellets were formed into 150 μm by compression molding using a heated hydraulic press (Carver, Inc.). The processing temperature was 140°C with 5 tons of pressure for every 25 g. of pellets
3. The assembly (CFRP + EAA barrier layers) was placed on a Teflon-coated aluminum tool plate. The parts were covered with a Teflon release film. The plate was then wrapped in a vacuum bag, similar to composite manufacturing. Vacuum was applied inside the bag so that 1-atm pressure compressed on the tool plate. The assembly was soaked inside an oven at 150°C for 30 minutes.
4. Edge filling frames were also made by compression molding the EAA pellets into 1.5 mm thick sheets using the same process conditions. A 0.75 mm thick Teflon block was used during the compression molding process to mold the electrolyte filling channel into the frames. The sheets were then cut into the pre-designed dimensions with steel rule dies using a pneumatic die cutter.
5. The materials were allowed to dry in a vacuum oven for >48 hours at 50°C prior to each step.

Assembly and Riveting Process

1. EAA cylinders were injection-molded using a benchtop plastic injection molding machine (Medium Machinery, LLC). The process temperature was 160°C.
2. A placeholder 1.5 mm aluminum insert was placed inside the electrolyte channel during the assembly/riveting process to ensure the electrolyte channel was not blocked.
3. The assembly was compression-molded between a pair of Teflon-coated aluminum tool plates inside a heated hydraulic press (Carver, Inc.). The laminate was pressed at 100°C and 0.5 MPa pressure for 5 minutes.

4. The assembled cells were allowed to cool down to room temperature before removing the aluminum inserts.
5. Samples were frequently cut to reveal the cross section in order to inspect if the rivets completely melted, filled the void, and fused to the facesheets.
6. The materials/assembled cells were allowed to dry in a vacuum oven for >48 hours at 50°C prior to each step.

Electrolyte Filling / Degassing / SEI Formation

1. The electrolyte filling took place inside an argon-filled glovebox.
2. 10mL $LiPF_6$ in EC/DMC/DEC organic solvent was filled using a micro-pipette through the electrolyte filling channel. The filled cells were let sit overnight to allow electrolyte absorption.
3. The electrolyte filling channel is temporarily sealed using a heated bar sealer.
4. The SEI formation consisted of a C/10 charge + 24-hr CV hold at 4.2V.
5. The electrolyte filling pocket was cut open to allow residual gas to escape (degassing) under brief vacuum.
6. The electrolyte channel was trimmed at the edge of the CFRP facesheet. A rectangular EAA insert was placed inside the channel. The edge was then permanently sealed again with a heated bar sealer.

Expanding MESC Design Space:

D_{eff} is scale-dependent, and particularly for a multi-material member, the value depends on the modulus, cross-section, and the spatial distribution of individual parts. D_{eff} of a sandwich structure increases with the square of the distance of the facesheets from the neutral axis. As such, efficient sandwich structures place a stiffer material, or facesheets, towards the outer surfaces where bending stresses are maximum, and separate them as far from each other as possible. However, the relatively small battery-to-facesheet thickness ratio of first generation MESC were limited by the preliminary, non-automated fabrication process. Therefore, first-generation cells were merely sufficient for a qualitative comparison. As our manufacturing capabilities become more mature, D_{eff} of the MESC can be significantly improved by increasing the thickness of the battery core with respect to the facesheet thickness, which simultaneously improve the cell energy density.

Effects of Rivet Density on Core Shear Modulus

Figure S9 shows the effective shear modulus of the core (G^*_c) of each experimental sample type (*CFRP/No Rivets, MESC 4×4, MESC 5×5,* and *Ideal Structural Sandwich*) as a function of their corresponding rivet volume fraction in the electrode stack ($\upsilon_{f,\,rivet}$). The effective core shear modulus (labelled 'Experimental Data' in Figure S9) was back-calculated via Equation 1 (in main text) using the measured bending rigidity values, geometric dimensions, and CFRP's mechanical properties. We then obtained a first-pass empirical function (labelled 'Empirical' in Figure S9) to describe the relationship between G^*_c and $\upsilon_{f,\,rivet}$. As more rivets are added, the interlayer slippage is increasingly inhibited. In other words, it is expected that the inherent, shear-slipping-prone mechanical properties of the electrodes are increasingly overtaken by those of the more rigid rivets. At either extreme ($v_{f,\,rivet} = 0$ and $v_{f,\,rivet} = 1$), the properties of the core approach those of the non-interlocked electrodes and the bulk properties of the rivets' polymer material,

respectively. Therefore, we assumed the combined effect on the G^*_c increase comes from the superposition of two effects: 1) logarithmic increasing contribution of the rivets' interlocking and 2) logarithmic decreasing contribution of the stack which is prone to interlayer slippage. This combined effect is shown in the equation below:

$$G_c^* = G_{c,no\ interlock}^* e^{-16.4 v_{f,rivet}} + G_{c,polymer}^* (1 - e^{-16.4 v_{f,rivet}})$$

where $G^*_{c,\ no\ interlock}$ is the intrinsic slippage-prone shear modulus of the non-riveted configuration, which was found to be 10.1 MPa, $G^*_{c,\ polymer}$ is the bulk shear modulus of the rivets' polymer material (EAA), which is 66.7 MPa. The actual relationships between these parameters are more complex and depend on the rivet diameter to spacing ratio, rivet patterns (square, rectangular, triangular, or randomized grids), and their mechanical interaction. While this will be addressed in detail in the follow-up publication, the current empirical function serves to help us understand the design parameterization space and resulting estimated performance of MESC with different configurations. Nevertheless, the empirical function captures the experimental results of this study reasonably well, and most importantly, explains the non-linear stiffening effect upon adding more rivets.

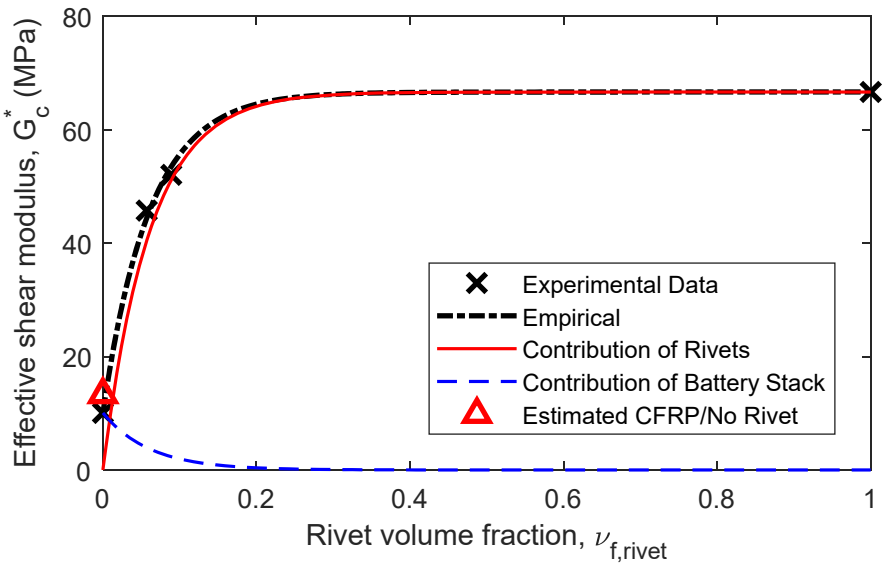

Figure S 9. Effects of $\upsilon_{f,\,rivet}$ on the core's G^*_c comparing the experimental data and the fitted empirical function.

Since no interlocking is present in the *CFRP/No Rivets* cells, we can further break down its core's effective shear modulus ($G^*_{c,\,no\ interlock}$) into a linear combination of its constituent components. That is, $G^*_{c,\,no\ interlock}$ is merely an area-weighted average of the shear modulus of the battery stack and the contribution from the frame by the bulk properties of the EAA.

$$G^*_{c,no\ interlock} = G^*_{c,battery}\left(\frac{w_{batt}}{w_{cell}}\right) + G^*_{c,polymer}\left(\frac{w_{frame}}{w_{cell}}\right)$$

$$G^*_{c,no\ interlock} \simeq G^*_{Baseline\ Pouch\ Cell}\left(\frac{w_{batt}}{w_{cell}}\right) + G^*_{c,polymer}\left(\frac{w_{frame}}{w_{cell}}\right)$$

where $G^*_{c,\,battery}$ is shear modulus of the battery stack, and w_{batt}, w_{frame}, and w_{cell} are the widths of the battery stack (90 mm), edge-filling frame (20 mm), and the combined width (110 mm), respectively. The experimental shear modulus of the *Baseline Pouch* cells, $G^*_{c,\,Baseline\ Pouch\ Cell}$, calculated using Equation 1

(main text) can be used to approximate $G^*_{c,\ battery}$ (i.e., $G^*_{c,\ battery} \approx G^*_{c,\ Baseline\ Pouch\ Cell}$). The calculated $\hat{G}^*_{c,\ no\ interlock}$ is plotted as a red triangle in Figure S9 which matches reasonably well with the actual $G^*_{c,\ no\ interlock}$ obtained from the *CFRP/ No Rivets* cells. This shows that without the interlocking rivets, the battery core's mechanical properties converge to those of typical *Baseline Pouch* cells.

Energy Density and Bending Rigidity of MESC with Varying Core Thickness, Rivet Density, and Facesheet Thickness

Similar to optimizing ply orientation for composite laminates, MESC present a new material design and optimization problem that gives engineers flexibility to tailor the material according to the requirements of the intended application. Mechanical and electrical performance of MESC depend on the facesheet thickness (t), battery core thickness (c), and, as emphasized in the main text, the rivet volume fraction ($\upsilon_{f,\ rivet}$), among many other. The following parametric study shows the variation in 1) gravimetric energy density, 2) volumetric energy density, and 3) flexural rigidity (D_{eff}), as a function of the three aforementioned design variables.

In Figures S10A and B, the gravimetric and volumetric energy densities are estimated by considering the volume and mass fractions of the functional electrode material, multiplied by the intrinsic energy density of the battery. The volume and mass fractions of each design are a function of t, c, and $\upsilon_{f,\ rivet}$. Figure S10C shows the bending rigidity as a function of t, c, and $\upsilon_{f,\ rivet}$ as calculated using Equation 1 (in main text), by assuming that, for a given $\upsilon_{f,\ rivet,}$ G^*_c is invariant with respect to t and c. Table S5 summarizes the estimated parametric results due to doubling and tripling the stack thickness while maintaining the rivet volume fraction and facesheet thickness.

Table S 4. Increase in gravimetric energy density, volumetric energy density, and bending stiffness from doubling and tripling the stack thickness for MESC cells with the same rivet volume fraction and facesheet thickness as the MESC 4×4 studied in this work.

Core Thickness, c (mm)	Gravimetric Energy Density (Wh/kg)	Volumetric Energy Density (Wh/L)	Bending Rigidity ($N.m^2$)
c = 3.4 mm (this study)	131	260	11
c = 6.8 mm	146	307	24
c = 10.2 mm	154	327	38

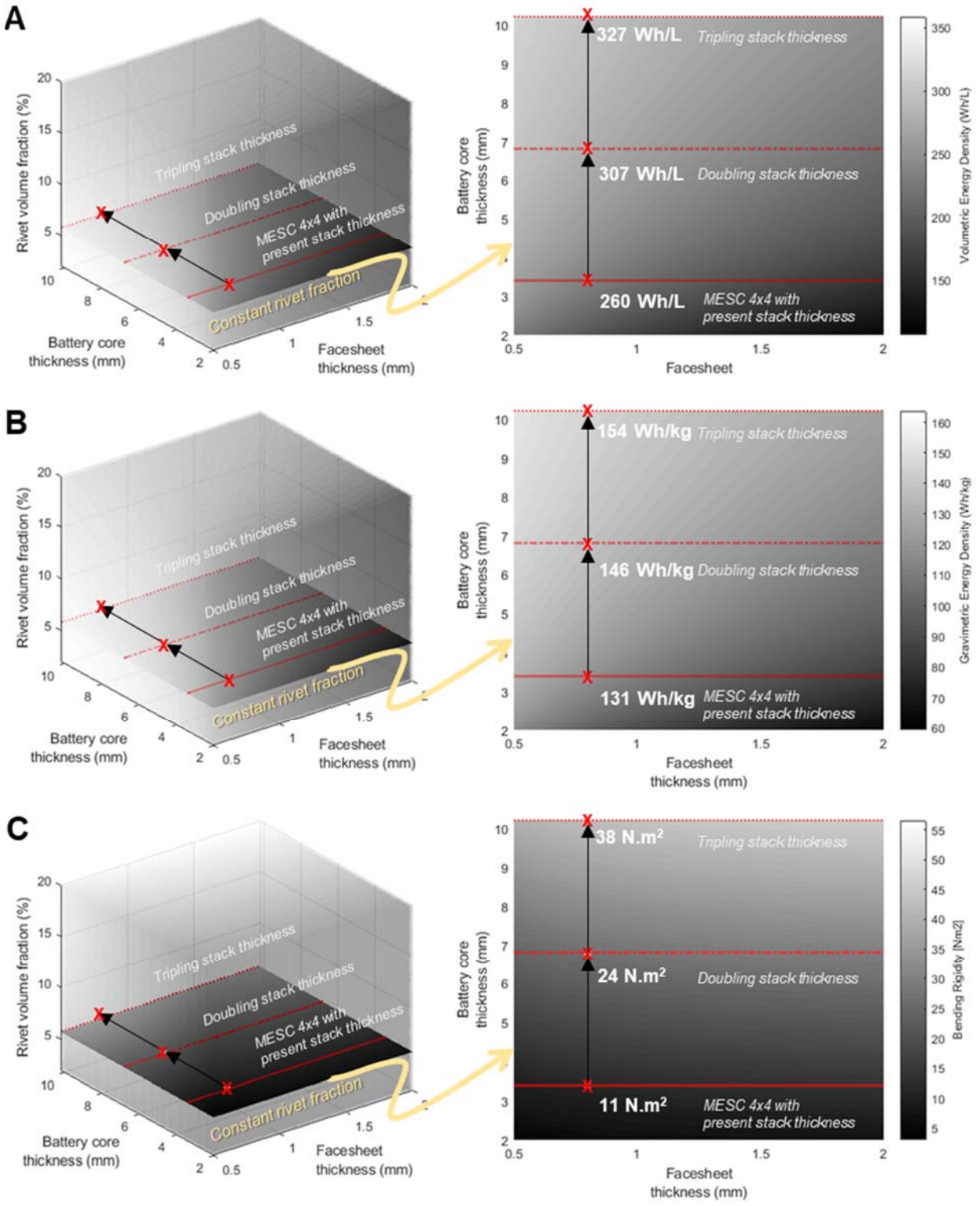

Figure S 10. Parametric results showing the estimated A) volumetric energy density, B) gravimetric energy density, and C) effective bending rigidity as a function of facesheet thickness, core thickness, and rivet fraction.

Supplementary References:

- Chang, Fu Kuo, Raphael Gerard Christian Nardari, and Purim Ladpli. "Multifunctional energy storage composites." U.S. Patent Application No. 15/549,117.